NASA CR 111924

MASTER AGREEMENT
TASK ORDER FOUR

Particle Dislodgement and Entrainment by a Low Density Airstream Flowing Over a Surface

By R.K. Weinberger and G.L. Adlon

Prepared Under Contract No. NAS 1–8137 by

MCDONNELL DOUGLAS ASTRONAUTICS COMPANY–EAST

Saint Louis, Missouri 63166 (314) 232–0232

for

NATIONAL AERONAUTICS AND SPACE ADMINISTRATION

Particle Dislodgement and Entrainment By a
Low Density Air Stream Flowing Over a Surface

TABLE OF CONTENTS

(CONT'D)

LIST OF FIGURES AND TABLES

LIST OF PAGES

NOMENCLATURE

A	Surface area
F_b	Aerodynamic force on surface model bottom
F_s	Aerodynamic force on surface model support struts
F_t	Aerodynamic (tangential) force on test surface
F_T	Total aerodynamic force on exposed system
ℓ_o	Initial position of entrained particle (=0)
ℓ_1	Position of entrained particle at time t_1
P_i	Air flow impact pressure
P_s	Air flow static pressure
$P(q_\infty)$	Probable experimental error in the air flow dynamic pressure
$P(\bar{V}_p)$	Probable experimental error in the particle average threshold departure velocity
$P(\tau_t)$	Probable experimental error in the aerodynamic shear stress
q_∞	Air flow dynamic pressure
R	Universal gas constant
R_x	Surface Reynolds number based on initial surface roughness from leading edge ($=19.96\left(\frac{x}{\epsilon}\right)^{.46}$)
S	Constant ($=225^\circ R$ for air)
T_∞	Air flow temperature ($^\circ R$)
T_o	Reference absolute temperature ($=492^\circ R$)
t_o	Initial time (=0)
t_1	Final time
V_∞	Air flow velocity
$\bar{V}_p$	Particle average threshold departure velocity
x	Distance of initial surface roughness from leading edge
γ	Ratio of specific heats (=1.4 for air)

Particle Dislodgement and Entrainment By a Low Density Air Stream Flowing Over a Surface

$\Delta\ell$	Particle displacement
Δt	Elapsed time (=2.84 milliseconds)
δF_t	Uncertainty or error in F_t
$\delta \ell_o$	Uncertainty or error in ℓ_o
$\delta \ell_1$	Uncertainty or error in ℓ_1
δP_i	Uncertainty or error in P_i
δP_s	Uncertainty or error in P_s
δq_∞	Uncertainty or error in q_∞ (=P(q_∞))
δt_o	Uncertainty or error in t_o
δt_1	Uncertainty or error in t_1
ϵ	Height of sharp roughness
μ_o	Reference absolute viscosity (=0.35 x 10^{-6} lb_f sec/ft^2)
μ_∞	Air flow viscosity
ρ_∞	Air flow density
τ_t	Aerodynamic shear stress

ROBERTS' NOMENCLATURE (APPENDIX C)

a	Momentum factor
C_f	Coefficient of friction
c	Soil packing constant
q	Gas flow dynamic pressure
t	Time
u	Gas radial velocity
y	Depth of soil erosion
β	Soil surface slope
σ	Soil mass density
τ	Aerodynamic shear stress acting on the surface

τ^*	Surface shear stress or resistivity

BAGNOLD'S NOMENCLATURE (APPENDIX D)

A	Constant equal to 0.1 for air
d	Particle diameter
g	Acceleration of gravity
k	Surface roughness parameter
V_*	Wind "shear velocity"
V_{*_t}	Wind "threshold shear velocity"
v	Wind velocity
z	Height above surface
ρ_∞	Wind density
σ	Particle material density
τ	Shear stress

Particle Dislodgement and Entrainment By a Low Density Air Stream Flowing Over a Surface

1.0 SUMMARY

This report describes the investigation of aerodynamic surface erosion conducted by McDonnell Douglas Astronautics Company—East under NASA contract NAS1-8137[1].

An experimental technique was developed and a preliminary investigation made of the dislodgement and subsequent entrainment of solid particles by a stream of low density air flowing over a particulate surface. Four size ranges of solid particles and two surface profiles were tested. At the inception of surface erosion the following were determined: airstream dynamic pressure, airstream density, aerodynamic shear stress on the surface and/or surface resistivity, particle departure angle, and particle departure velocity. In addition, the entrained particles were trapped at several heights above the surface and the size distributions determined.

The data indicate that the dynamic pressure of the airstream required to dislodge particles increases with the average particle size. There was, however, no systematic trend showing a change in threshold airstream conditions with a very large change in surface roughness. Particles were observed to leave the surface with a very large range of velocity vectors. Particle spin was also observed. The saltation layer particle size distribution had no apparent systematic change with height above the surface.

2.0 INTRODUCTION

When rocket-powered vehicles descend to, ascend from, or travel over a surface, the impingement of the exhaust gases on that surface can be detrimental. The area of immediate interest to the present Apollo and future Viking programs is that of the hazards of soil ejecta set into motion by the action of the rocket exhaust plume on the surface. The potential hazards of such ejecta[2] include visibility degradation, landing site alteration, experiment contamination, and vehicle damage, all of which were experienced, to some degree, by the recent Apollo landings on the lunar surface.[3-5] As a result of these potential dangers, a more complete understanding of surface erosion and particle entrainment is necessary to insure the success of future planetary exploration.

The mechanism of aeolian surface erosion has received considerable attention in view of its importance in the problems of air pollution and soil conservation,[6-18] and recently, in view of its importance in vertical take-off and landing vehicle degradation.[19-20] As a result, there is a certain amount of experimental information which is useful to the knowledge of extraterrestrial surface erosion even though there are significant differences in flow field conditions due to atmospheric differences.

More recently, several experimental and theoretical investigations have been conducted on the mechanism of dust entrainment by the impingement of a simulated rocket exhaust plume at vacuum conditions.[21-27] These studies provide information on the flow field of a highly underexpanded exhaust gas impinging on a dust-covered surface and a theoretical picture of the resulting dust entrainment.

Earlier work at McDonnell Douglas demonstrated that the lift/drag ratio of forces on a particle entrained in an air flow and the threshold velocity for a

particle-covered surface exposed to an air flow could be determined for a flow field expanding into a low static pressure.[28-30] However, no attempt was made at that time to investigate the surface particle entrainment mechanisms initiated by the low density parallel air flow.

This report describes an experimental study which was undertaken to provide some physical insight into the dislodgement and entrainment of solid particles from a surface by a stream of low density air flowing over the surface. The McDonnell Douglas Surface Erosion Simulator was used for the study because it could be operated at a low airstream density. Emphasis was placed on the airstream conditions at the inception of particle dislodgement and the motion of the dislodged particles. Anticipated application of the results are in the area of erosion of planetary surface by a descent braking engine or natural winds.

3.0 PROBLEM DEFINITION AND APPROACH

3.1 DEFINITION OF PROBLEM. The present investigation is part of an overall analyses, design, and fabrication of impact test vehicles for planetary landing. This study is primarily concerned with an experimental investigation of surface erosion to provide a more complete description of the erosion mechanism, to supplement existing erosion theories, and to provide a basis for future work.

Experimental test parameters simulate the lunar surface particle size, surface roughness, and lower range of radial gas flow dynamic pressure that the surface is exposed to during a Lunar Module powered descent. In addition to the above, the test parameters are similar to those of the environment theorized to be conducive to dust erosion on the surface of Mars by local winds.

3.2 EXPERIMENTAL APPROACH. The objectives of this investigation were to define the following surface erosion parameters:

- Threshold dynamic pressure
- Threshold surface shear stress
- Particle threshold departure velocity
- Particle threshold departure angle
- Particle saltation height and size distribution
- Surface particle size effect
- Surface roughness effect
- Entrainment phenomena by photography

The gas-flow-surface interaction was simulated by exposing a 9-inch wide x 16-inch long particle surface to a parallel air flow of dynamic pressure up to 1.5×10^{-2} pounds/inch^2 expanding into a static pressure ranging from 0.25 to 15

torr. This simulation was performed in the McDonnell Douglas Surface Erosion Simulator which has a 9.6-inch wide x 14.5-inch high x 48-inch long test section. The air flow field in this test section was stable and easily identifiable with respect to boundary layer formation.

The study of surface erosion due to a parallel gas flow at low static pressures required the following capabilities:

- Simulation of a gas flow field
- Simulation of a geological surface
- Analyses of the aerodynamic forces on a test surface
- Photographic recording of particle entrainment
- Analyses of a saltation layer

3.2.1 FACILITY DESCRIPTION. The wind tunnel used for the experimental study is contained within a 9 x 11 x 20 foot high-altitude chamber (Figure 1). The gas pumping system, which is a six-stage noncondensing type steam ejector, is used to maintain low static pressures during controlled air flow over the test surfaces. Air is metered into the wind tunnel plenum chamber, where it passes through two 20-mesh screens (with 0.016-inch diameter wires and 0.034-inch wide openings and separated approximately 1 inch) to reduce flow turbulence. The plenum chamber converges to a 9.6-inches wide by 14.5-inches high tunnel. Distance from initial convergence to the tunnel test section is 89.5 inches. Within the tunnel is a honeycomb-shaped laminar flow element which further reduces flow turbulence before it enters the tunnel test section. The test section itself is a glass tunnel 9.6-inches wide, 14.5-inches high, and 48-inches long (Figure 2). A typical velocity profile of the air flow in the test section is shown in Figure 3.

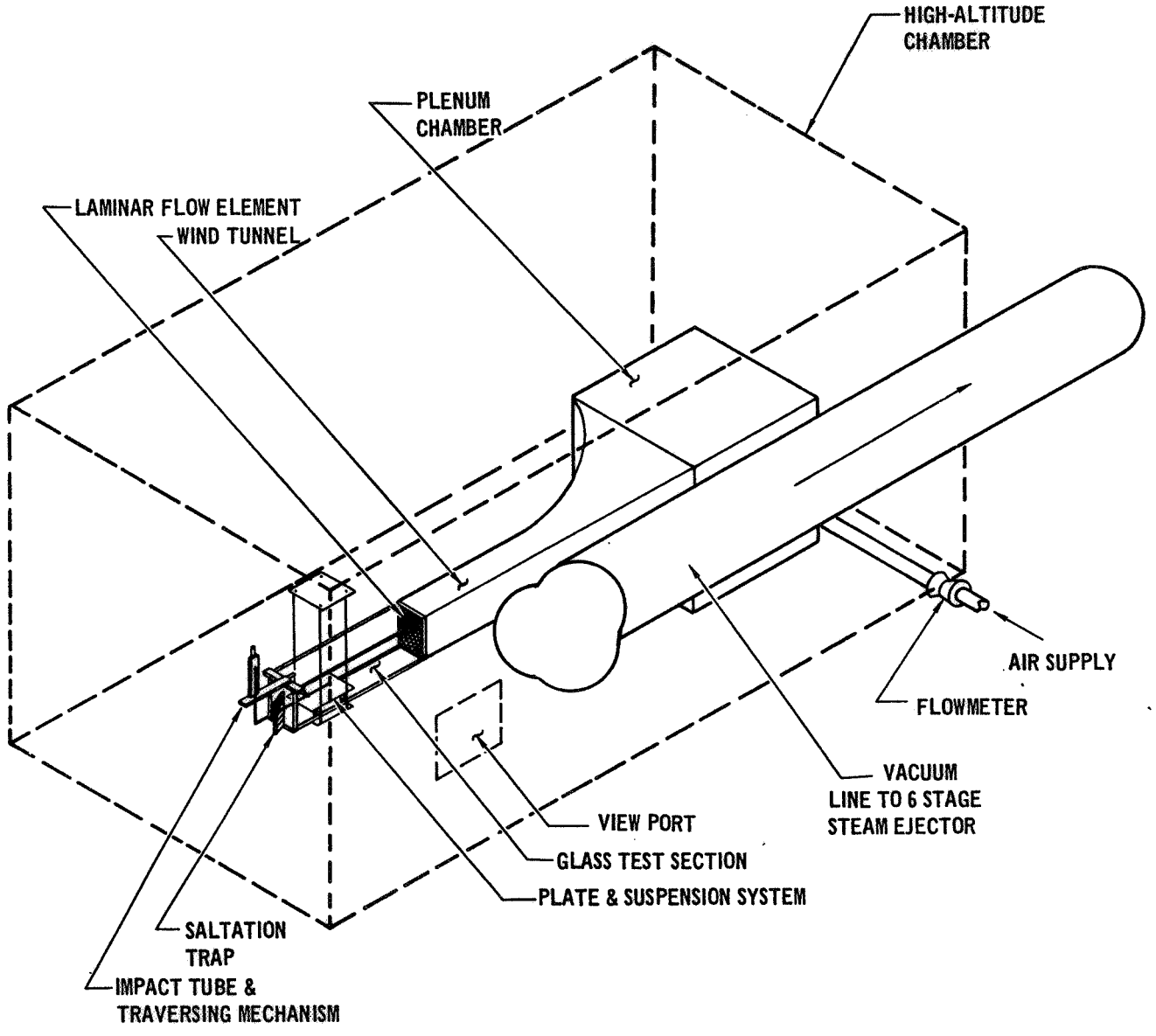

FIGURE 1 MCDONNELL DOUGLAS SURFACE EROSION SIMULATOR

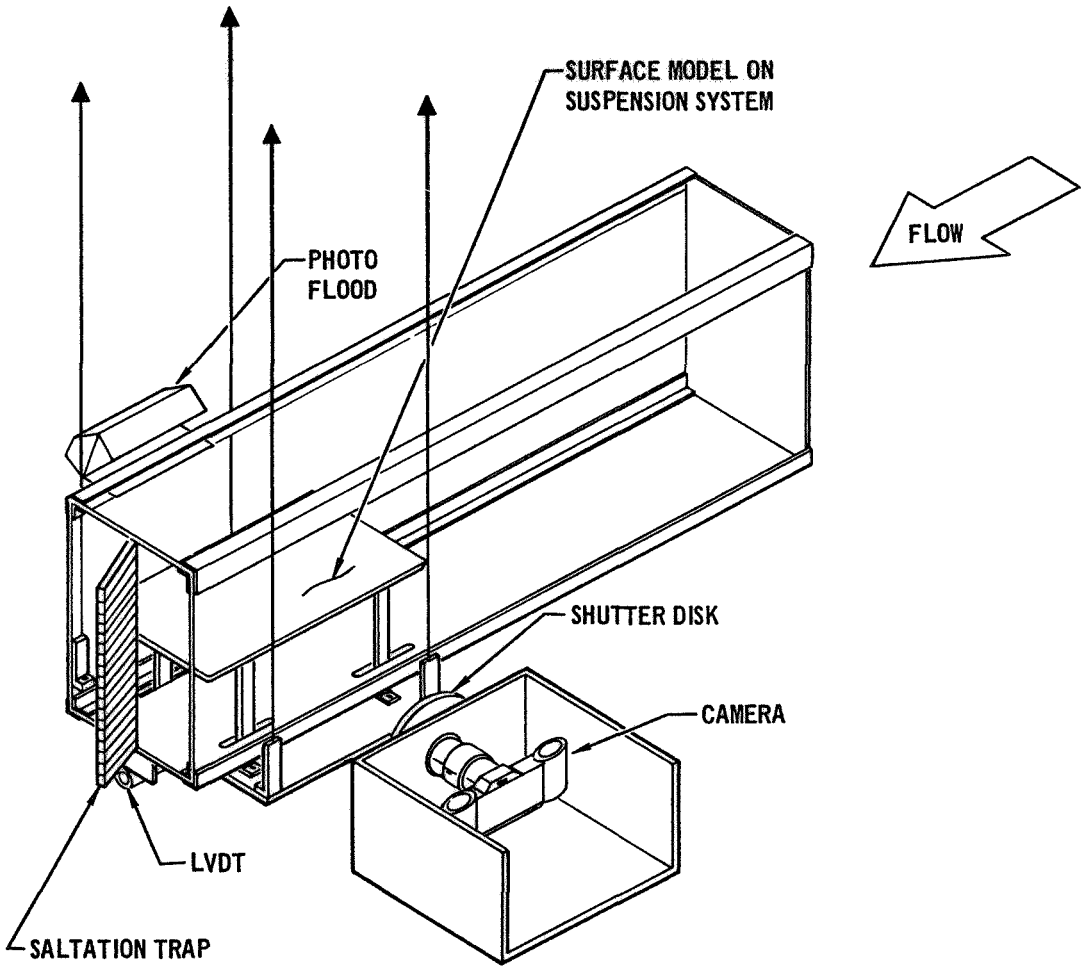

FIGURE 2 WIND TUNNEL TEST SECTION AND SUPPORT SYSTEMS

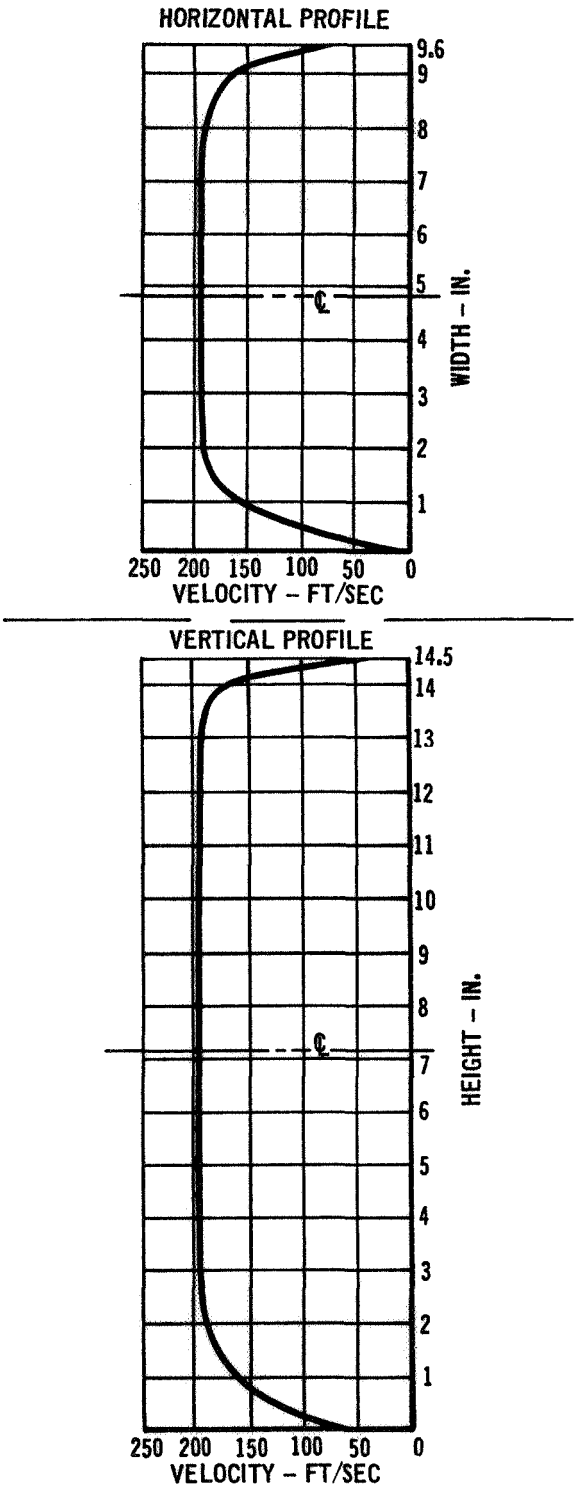

FIGURE 3 TYPICAL VELOCITY PROFILE IN TEST SECTION

Air used for generating gas flow in the tunnel is drawn from the McDonnell Douglas Polysonic Wind Tunnel supply tanks. This air is dried to a dew point of -20 to -40°F. Variation in the gas flow dynamic pressure is achieved by adjusting the metered air flow to the tunnel and throttling the chamber exit flow with a butterfly valve in the 30-inch diameter vacuum line leading to the steam ejector.

Air flow in the tunnel is measured with an impact tube probe attached to a remotely-operable, motor-driven mechanism having 3 degrees of motion (Figure 4). The differential (impact pressure) which exists between the total and static pressures is measured with a 1-torr (1 mm of mercury) range diaphragm-type electric manometer. Chamber static pressure is monitored with a 100-torr range unit. Copper-constantan thermocouples are used to measure temperature at critical points in the air flow.

3.2.2 GAS FLOW. Because the very high vacuum (10^{-9} torr) at the lunar surface cannot be achieved in the high-altitude chamber which is used for surface erosion simulation, the radial flow field dynamic pressure distribution of an exhaust plume was simulated. The quantitative values of these distributions were based on R. E. Hutton's application of Roberts' Flow Field Theory[31-33] using recent data obtained during the flights of Apollo 11 and 12. Experimental values consisted of generating air flow dynamic pressures up to 1.5×10^{-2} pounds/inch^2.

In cognizance of the applicability of this investigation to the growing concern towards dust erosion on the surface of Mars, the air flow static pressure was maintained in the realm of the theoretical atmospheric pressure of the Martian surface (3 to 15 torr).[34]

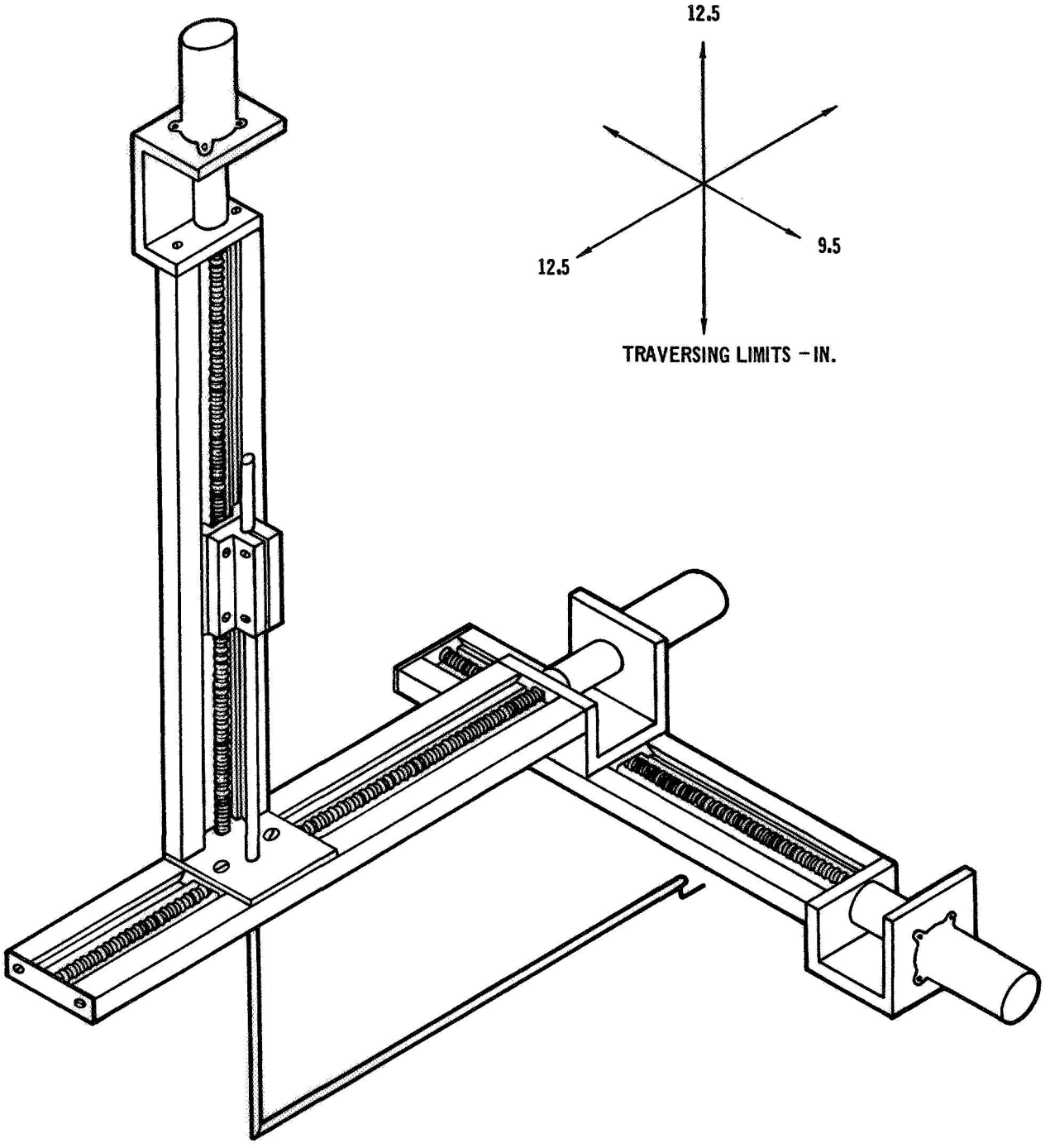

FIGURE 4 IMPACT TUBE AND TRAVERSING MECHANISM

3.2.3 SURFACE MODELS. The surface profiles and particle size range combinations were based on the analyses of topographic maps prepared from close-up stereo photographs of the lunar surface[35-39], and the lunar material obtained during the flights of Apollo 11 and 12.[40-41] A total of eight surface configurations, combinations of two surface profiles and four particle size distributions, were defined. The two surface profiles were a smooth surface configuration and a rough surface configuration having 3/8-inch high furrows. The particle diameters of the four size distributions were 1 to 500 microns, 177 to 210 microns, 53 to 63 microns, and 1 to 44 microns.

Aluminum oxide (Al_2O_3 with sp. gr. 3.97) was initially chosen as the surface particulate material because of its availability in the desired size distributions; however, as described in Section 4.4, it was replaced with silicon dioxide (SiO_2 with sp. gr. 2.66) because of inherent optical properties. The silicon dioxide was sieved to the desired size distributions before it was used as the surface particulate material. Comparison of the Apollo 11 bulk material and the 1 to 500 micron SiO_2 particulate material is shown in Figure 5.

Each surface was prepared in two ways--one that particle movement could not be initiated by the air flow, and the other that particle movement could be initiated. For clarity, the surface configurations prepared for no particle movement are called static surface models, and those prepared for particle movement are called dynamic surface models. A compilation of the surface models is given in Table 1. The static surfaces were studied to define the combined effect of surface roughness and particle size distribution on aerodynamic shear stress. Dynamic surfaces were studied to define the surface shear stress and/or surface resistivity at threshold conditions.

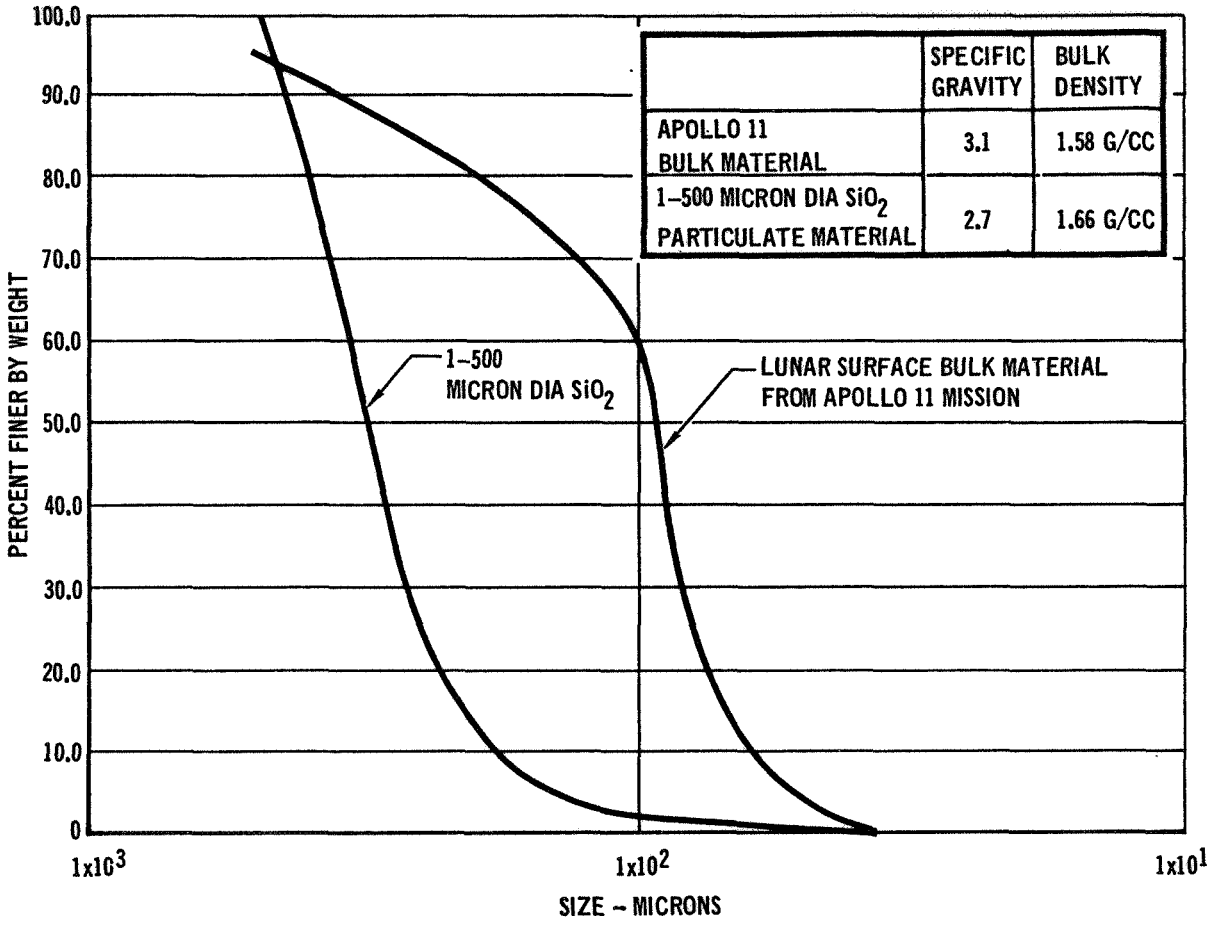

FIGURE 5 PARTICLE SIZE DISTRIBUTION

Particle Dislodgement and Entrainment By a Low Density Air Stream Flowing Over a Surface

Static surface models were prepared by fixing a thin layer of particulate material to the top surface of a 9-inch wide x 16-inch long flat aluminum plate having a 45 degree beveled leading edge. For the smooth surface profiles, this

TABLE 1
SURFACE MODELS

STRUCTURE	PARTICLE SIZE RANGE	PROFILE
STATIC	1-500	SMOOTH
		ROUGH
	177-210	SMOOTH
		ROUGH
	53-63	SMOOTH
		ROUGH
	1-44	SMOOTH
		ROUGH
DYNAMIC	1-500	SMOOTH
		ROUGH
	177-210	SMOOTH
		ROUGH
	53-63	SMOOTH
		ROUGH
	1-44	SMOOTH
		ROUGH

was accomplished by cementing a thin layer of the desired size range of SiO_2 particles to the flat plate. For the rough surface profiles, 11 furrows 3/8-inch high and 1-inch wide at the base were cemented to the flat plate prior to coating it with SiO_2 particles. (See Figures 6 and 7.) The 1 inch base of the furrows was defined by the angle of repose of the least cohesive particulate material--the 1 to 500 micron SiO_2. Dynamic surface models were prepared by spreading a layer of the desired size range of SiO_2 particles over its respective static smooth surface model and "raking" it to the desired profile--smooth or rough. The total weight and center of gravity of the suspension system was maintained at a constant value for each model surface.

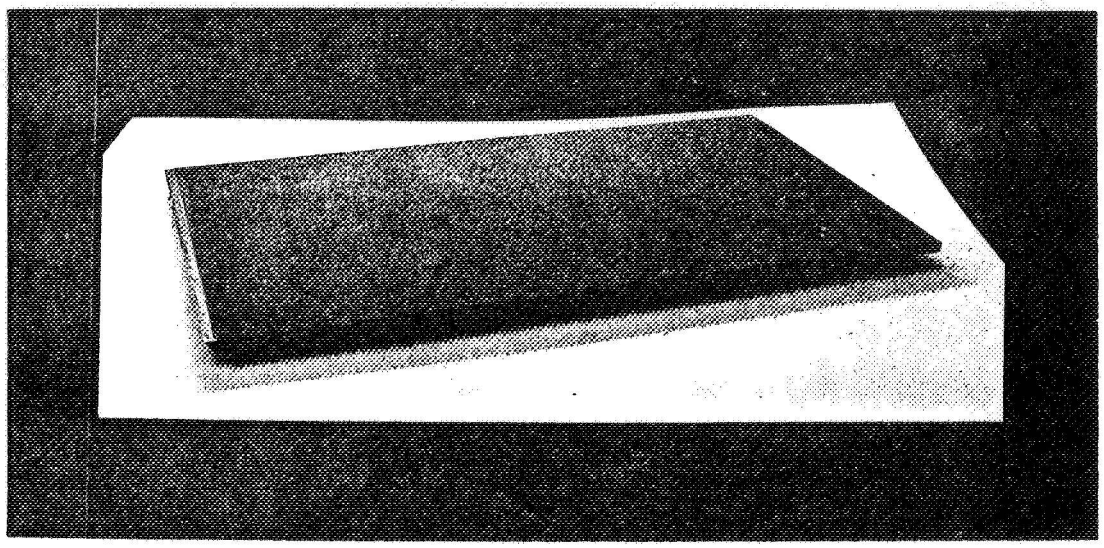

FIGURE 6 1 TO 500 MICRON DIA SiO_2 STATIC SMOOTH SURFACE MODEL

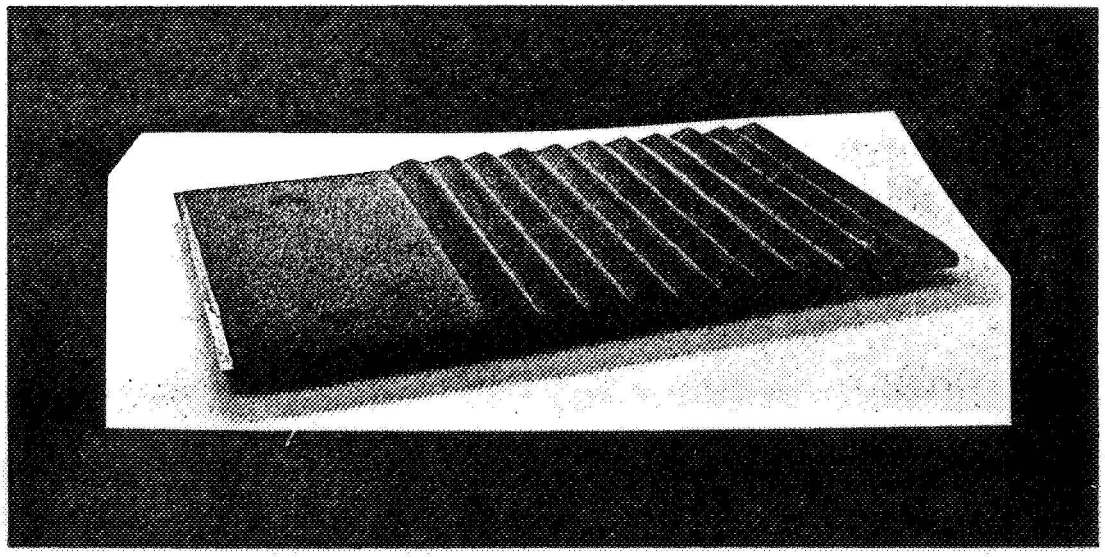

FIGURE 7 1 TO 500 MICRON DIA SiO_2 STATIC ROUGH SURFACE MODEL

3.2.4 SUSPENSION SYSTEM. The aerodynamic forces on a test surface were monitored as a function of surface displacement. The surface model was installed on a "pendulum-type" suspension system so that only the test surface and supporting struts were exposed to the air flow. The displacement of the surface model due to the aerodynamic forces of the air flow was then measured with a Schaevitz Engineering Linear Variable Displacement Transducer, Model 300 HR, located outside of the wind stream. (See Figure 2.) The core within the transducer was attached to the suspension system and was free to move within the transducer without restraint. The suspended weight was a constant for each test surface, and the system was calibrated prior to each test by measuring force versus surface displacement. The transducer output was fed into a recorder so that the displacement, recorded in 0.001 inch increments, was correlated with air flow dynamic and static pressure conditions. Any extraneous suspension system movement was dampened by a paddle which was attached to the bottom of the system and immersed in an oil-filled container.

3.2.5 PHOTOGRAPHIC SYSTEM. The surface entrainment phenomena were recorded by the photographic system shown in Figure 2. The camera is a 35 mm Nikon Model F body mounted on a 250-frame electric advance magazine. Initially a 200 mm lens extended 6-1/2 inches with a bellows attachment was used as the camera's optical system. However, the width- and depth-of-field were severely limited so it was replaced with a Micro-Nikkor F3.5, 35 mm lens (zero extension) which yielded a width- and depth-of-field of 7-5/16 inches and 1/4 inch, respectively. Panatomic-X film was used for its fine-gtain, high-resolution quality. The lighting is provided by a 1000-watt quartz-iodine lamp focused so that surface particle reflected (low angle) light into the camera optics. In order to record a time history of

the activity, a rotating shutter disk was positioned in front of the camera so that reflected light incident on the camera optics would be interrupted at a known rate. The result is a time base for each exposure.

3.2.6 TEST PROCEDURE. The procedure for conducting each test was essentially the same. The surface model was prepared and installed on the suspension system, and the suspended weight was measured. The system was then calibrated for aerodynamic drag by measuring surface displacement versus applied force. For dynamic models, a saltation trap was installed and the camera and lighting system prepared to record particle movement. The high-altitude chamber was then closed and evacuated. When the chamber test pressure stabilized, the air flow was initiated and parameter monitoring began. For the dynamic models, visual observation, via a telescope, was undertaken so that threshold conditions could be determined. The photographic system was manually operated at conditions of interest. Upon completion of the test, the air flow was terminated and the chamber repressurized to ambient conditions.

3.2.7 COMPUTATIONAL PROCEDURE. Threshold conditions and other inherent surface erosion parameters were measured and/or computed from experimental data for the eight surface configurations. For each test, the following experimental variables were required.

A. Flow Field Variables
    1. Air dynamic pressure
    2. Air density
    3. Air viscosity

B. Shear Stress Variables
    1. Surface model

2. Aerodynamic shear stress

3. Surface shear stress

C. Saltation Layer Variables (Dynamic models)

1. Particle departure velocity and angle

2. Particle size distribution

3.2.7.1 FLOW FIELD VARIABLES. The air flow dynamic pressure (q_∞) and velocity (V_∞) were determined as functions of the flow field impact pressure, static pressure, and temperature from the following Mach functions which are valid for low Mach Numbers:

$$q_\infty = P_S \left[\frac{\gamma}{\gamma-1} \left(\frac{(P_S + P_i)}{P_S} \right)^{\frac{\gamma-1}{\gamma}} - 1 \right] \quad (1)$$

and

$$V_\infty \ (\text{ft/sec}) = 49.1 \ (T_\infty {}^\circ R) \left[\frac{2}{\gamma-1} \left(\frac{(P_S + P_i)}{P_S} \right)^{\frac{\gamma-1}{\gamma}} - 1 \right]^{\frac{1}{2}} \quad (2)$$

Impact pressure (P_i) was monitored as the differential between the total and static pressure with an impact tube and 1-torr range diaphragm-type electric manometer, the static pressure (P_S) was monitored with a 100-torr range diaphragm-type electric manometer, and the temperature (T_∞) was monitored with copper-constantan thermocouples.

The air density (ρ_∞) was determined from the perfect gas law

$$\rho_\infty = \frac{P_S}{RT_\infty}$$

where the static pressure and temperature were monitored as described above.

The air viscosity (μ_∞) was determined as a function of temperature from Sutherland's equation

$$\frac{\mu_\infty}{\mu_O} = \left(\frac{T_\infty}{T_O} \right)^{1.5} \frac{T_O+S}{T_\infty+S} \quad (4)$$

where the reference absolute temperature (T_o) and absolute viscosity (μ_o) are 492^oR and 0.35×10^{-6} lb_f sec/ft^2, respectively. The value of S is a constant equal to 225^oR for air.

3.2.7.2 SHEAR STRESS VARIABLES. Each surface model was mounted on the suspension system prior to its set of experimental runs and leveled on both the x- and z- axes to within 0.25 degrees.

The aerodynamic shear stress (τ_t) on the test surface was determined as a function of the total aerodynamic force on that surface and the exposed areas of the suspension system by the relation

$$\tau_t \ (lb/in^2) = 6.94 \times 10^{-3} \ F_T \ (lb) - [2.50 \times 10^{-2} q_\infty (lb/in^2) + 1.96 \times 10^{-5}]. \qquad (5)$$

The total aerodynamic force (F_T) and air flow dynamic pressure (q_∞) were monitored as described in Section 3.2.4. It may be noted that the computed value of the aerodynamic shear stress in Equation 5 does not go to zero with the air flow dynamic pressure as one would expect. This is the result of curve fitted data and is explained more fully in Appendix A.

The surface shear stress or resistivity was also determined by Equation 5 using parameters observed at the inception of erosion.

3.2.7.3 SALTATION LAYER VARIABLES. The average departure velocity ($\bar{V}_p$) of an entrained surface particle was determined from the ratio of the particle displacement to elapsed time

$$\bar{V}_p = \frac{\ell_1 - \ell_o}{t_1 - t_o} = \frac{\Delta \ell}{\Delta t} \qquad (6)$$

The displacement ($\Delta \ell$) of a particle was measured directly from the photographic records of the saltation process with the initial position of the particle at the surface ($\ell_o = 0$). The elapsed time (Δ_t) was determined from the time base of those records.

Particle distribution in a saltation layer was determined as a function of height above the saltating surface. Entrained particles were caught in a trap, similar to the one used by Bagnold in his studies, located at the tunnel centerline downwind from the test surface. The trap itself was attached to the tunnel in such a way that it did not interfere with surface model displacement but effectively caught surface creep and entrained particles at predetermined increments above the surface. (See Figure 2.) Each vertical compartment sample was weighed to determine weight percent distribution relative to height and photomicrographed to determine size distribution relative to height.

3.2.7.4 PROBABLE ERROR. An error analysis (Appendix B) was employed to determine the propagating effect of flow field and surface parameter uncertainties on flow field dynamic pressure, aerodynamic shear stress, and particle departure velocity. To minimize error propagation, the following restrictions were imposed on each experimental test and the resulting data:

- Flow field parameters were stabilized before readings
- Surface model oscillation was dampened
- Only distinct particle tracks at the tunnel centerline were analyzed.

The uncertainties in the parameters needed to determine error propagation are listed below:

Parameter	Uncertainty
P_s	$\pm$ 9.67 x 10^{-4} lb/in^2
P_i	$\pm$ 1.934 x 10^{-5} lb/in^2
T	$\pm$ 2°F
F_T	$\pm$ 6.0 x 10^{-4} lb
ℓ	$\pm$ 1.3 x 10^{-3} ft

Parameter (Cont'd)	Uncertainty (Cont'd)
t	$\pm$ 2.0 x 10^{-5} sec

The average probable errors are presented in Table 2 below.

TABLE 2 AVERAGE PROBABLE ERROR

PARAMETER	AVERAGE PROBABLE ERROR
q_∞	$\pm 1.38 \times 10^{-5}$ LB/IN.^{2}
τ_t	$\pm 4.18 \times 10^{-6}$ LB/IN.^{2}
$\bar{V}_p$	$\pm 6.48 \times 10^{-1}$ FT/SEC

4.0 RESULTS AND DISCUSSION

Some difficulty was experienced in accurately repeating combinations of air flow dynamic pressure and surface model displacement; therefore, the data presented herein represent average experimental values.

4.1 FLOW FIELD.

4.1.1 AERODYNAMIC SHEAR STRESS.

4.1.1.1 UNCOATED POLISHED PLATE. A theoretical analysis of the drag or aerodynamic shear stress exerted on a flat plate[42] was performed and is compared to experimental data in Figure 8. The experimental shear stress on the uncoated polished plate is in close agreement with the theoretical analysis up to the point at which surface leading edge roughness generates downstream turbulence. This point is defined by a critical Reynolds number which is dependent on the distance of initial roughness from the plate leading edge and the roughness height[43]. In order to increase the critical Reynolds number, all surface models were prepared with initial roughness 0.25 inches downstream from the leading edge. For the uncoated polished plate, roughness height was based on surface paint thickness; for the surface models it was based on the largest particle diameter. The critical Reynolds number is given for all relevant data so that data validity is established.

4.1.1.2 SMOOTH AND ROUGH SURFACES. The aerodynamic shear stress exerted on the surface models is given as a function of air flow dynamic pressure in Figures 9 through 12. The aerodynamic shear stress varies randomly as the surface particle size decreases for both surface profiles. However, the numerical values of these variances are within the limits of the probable experimental error so the data may be misleading. That is, any relation between the aerodynamic shear

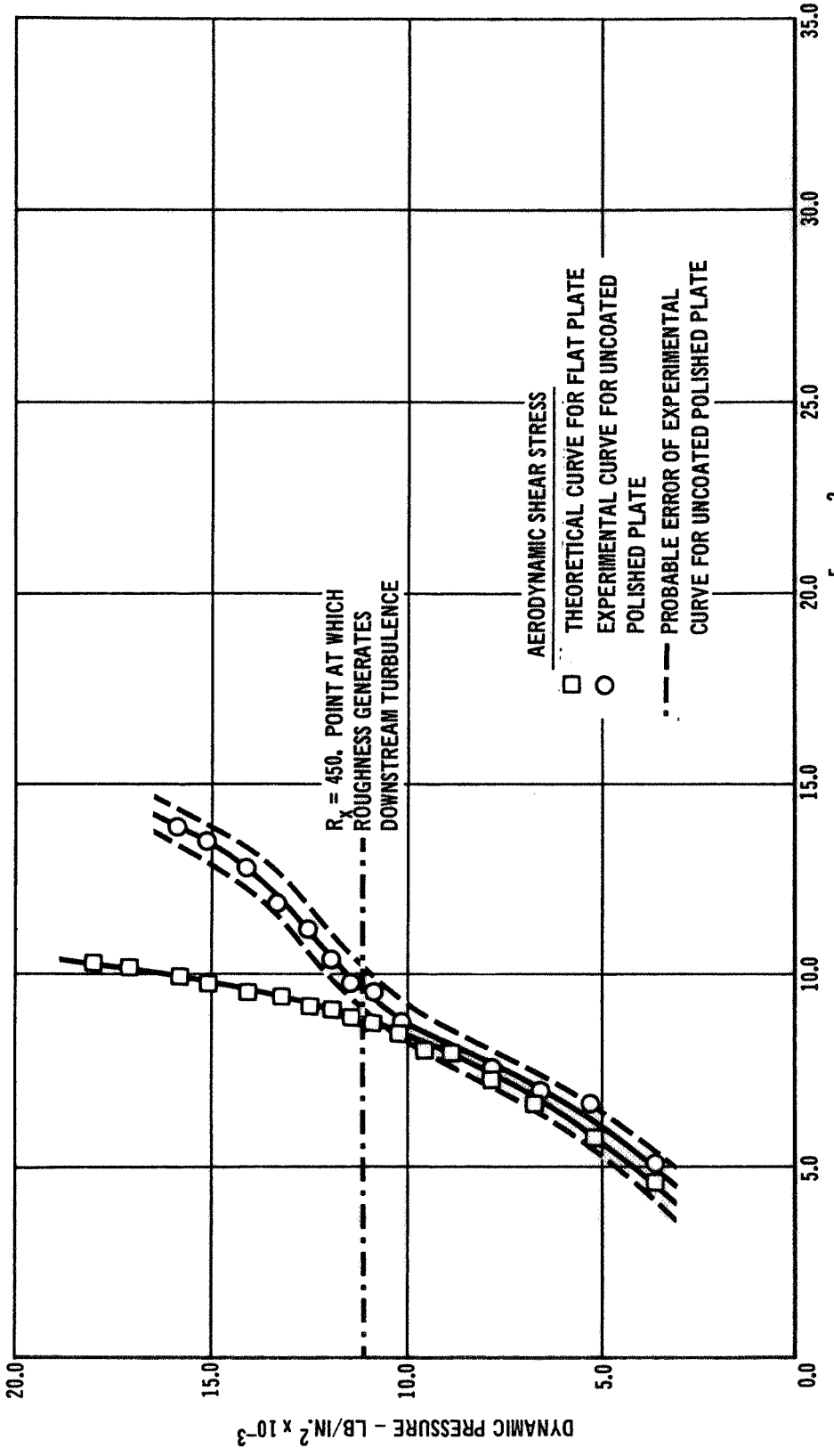

FIGURE 8 AERODYNAMIC SHEAR STRESS AND ERROR ANALYSIS – UNCOATED POLISHED PLATE

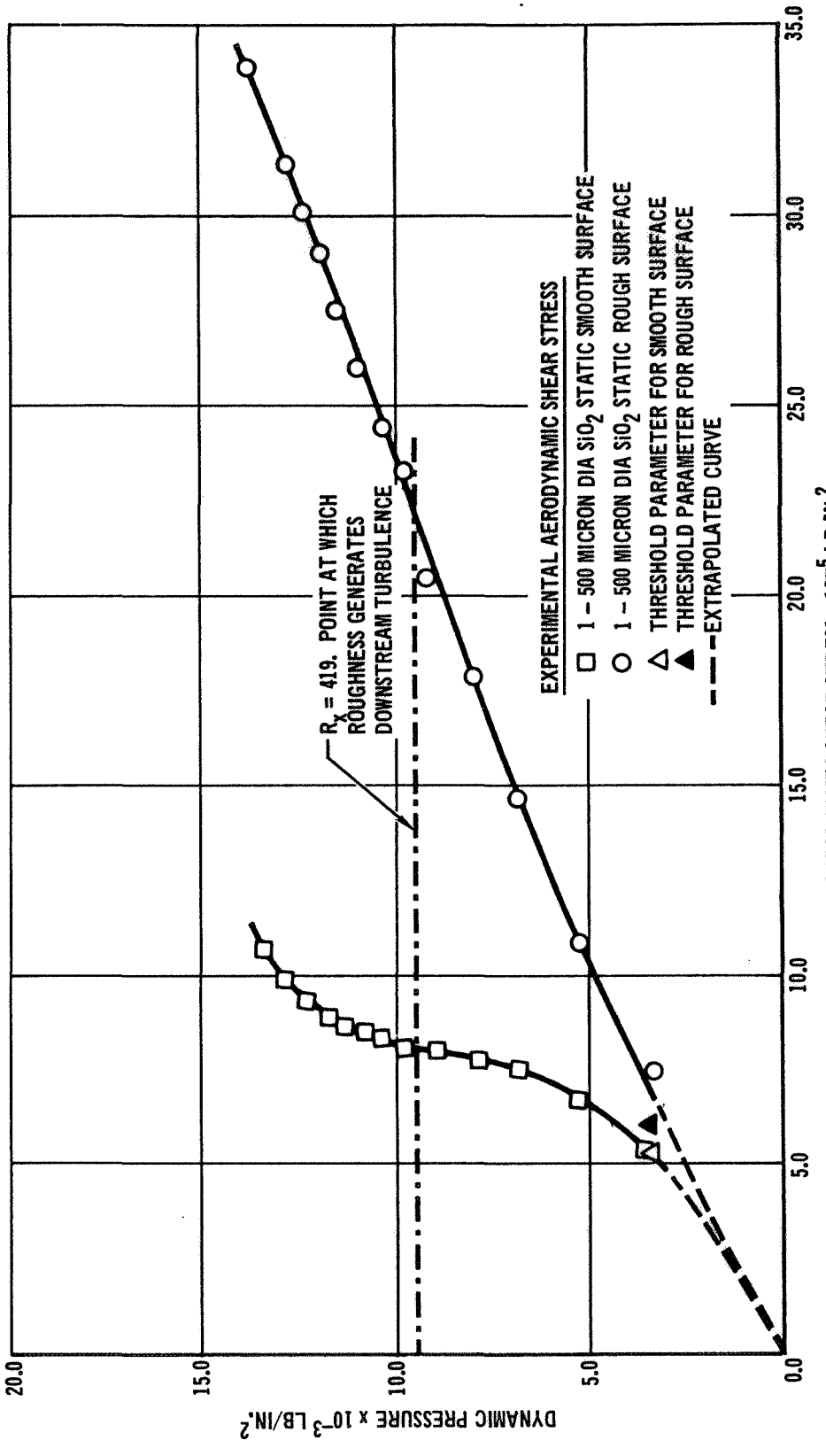

FIGURE 9 AERODYNAMIC SHEAR STRESS – 1 TO 500 MICRON DIA SiO_2

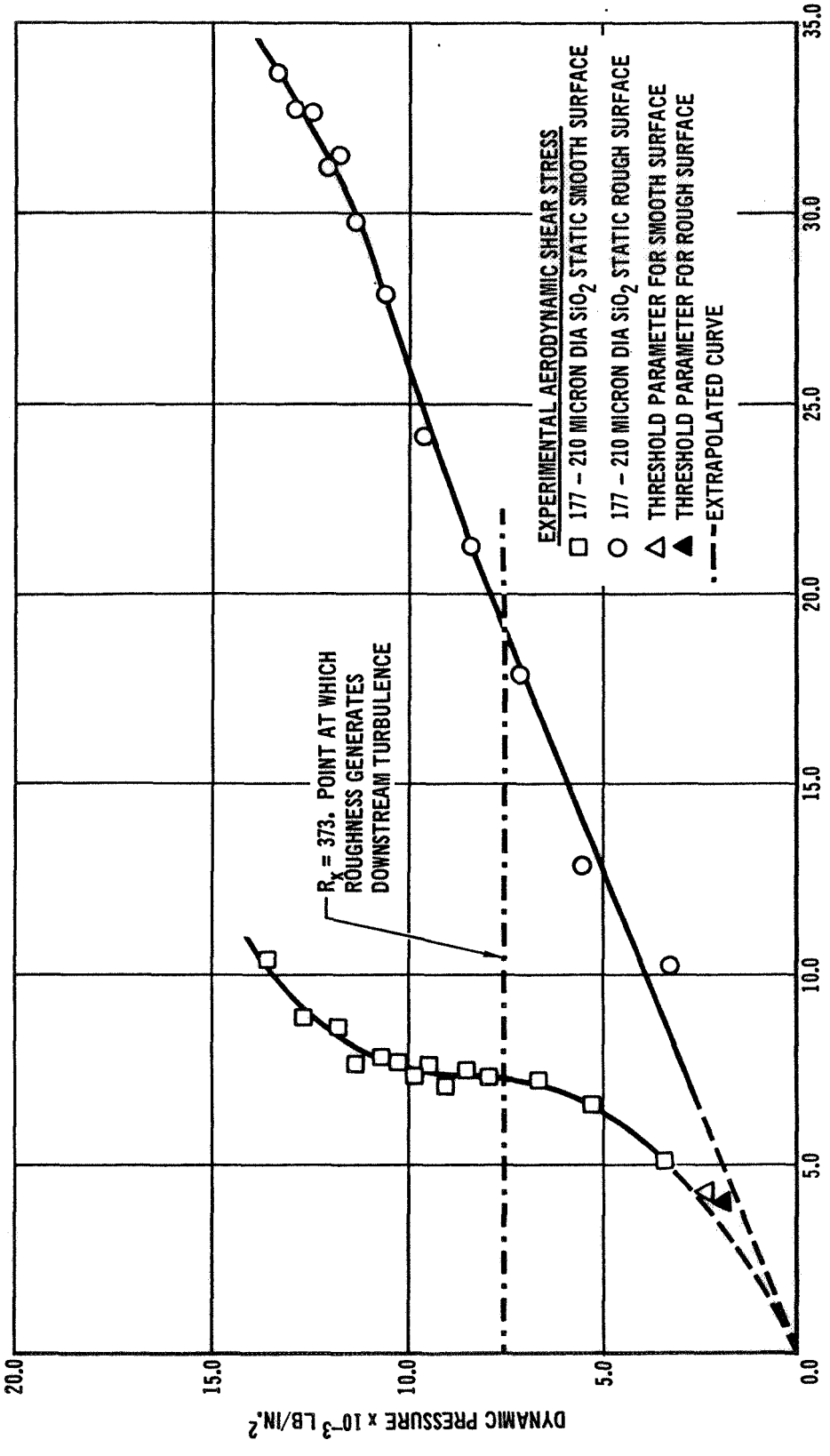

FIGURE 10 AERODYNAMIC SHEAR STRESS – 177 TO 210 MICRON DIA SiO_2

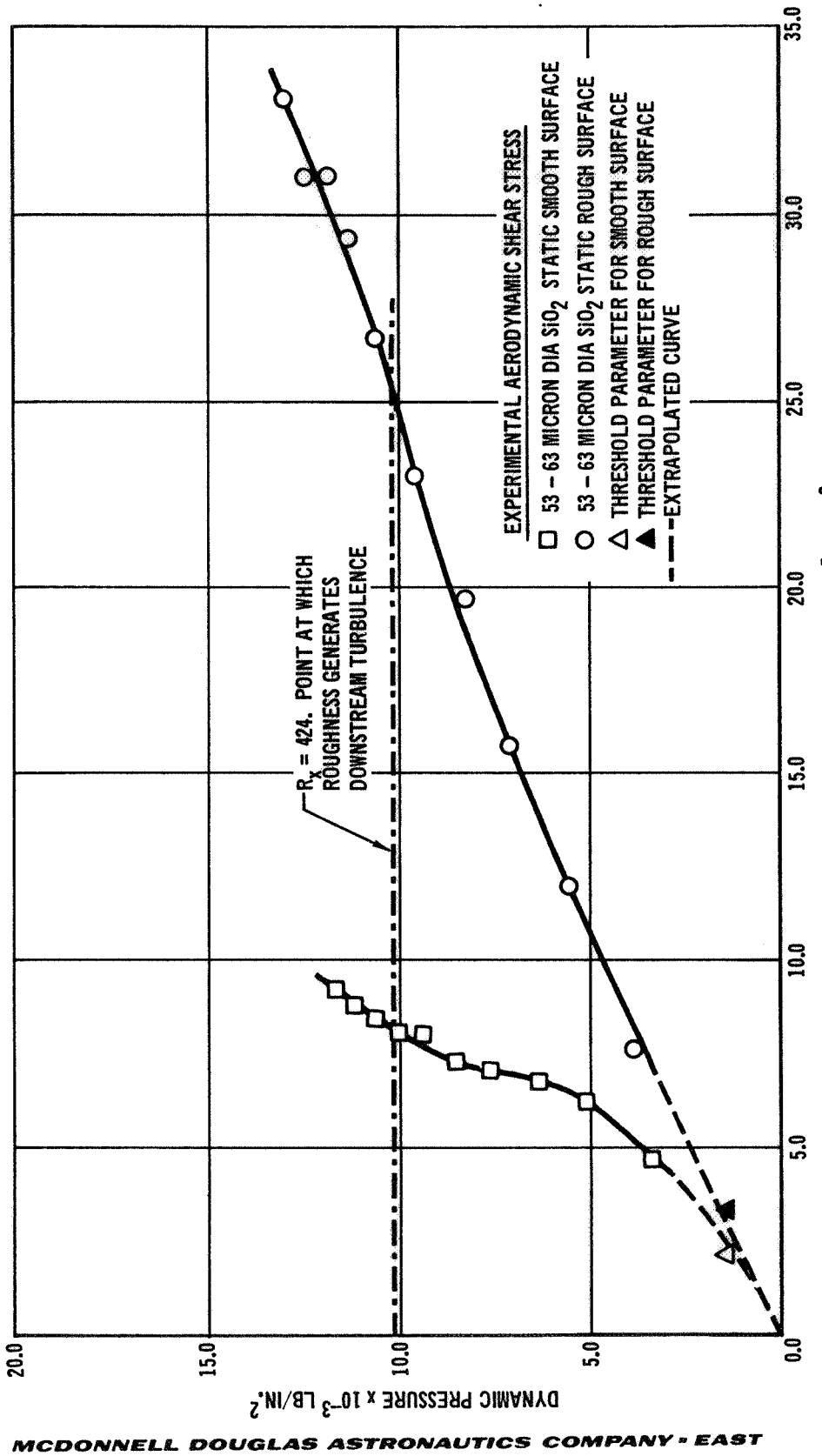

FIGURE 11 AERODYNAMIC SHEAR STRESS – 53 TO 63 MICRON DIA SiO_2

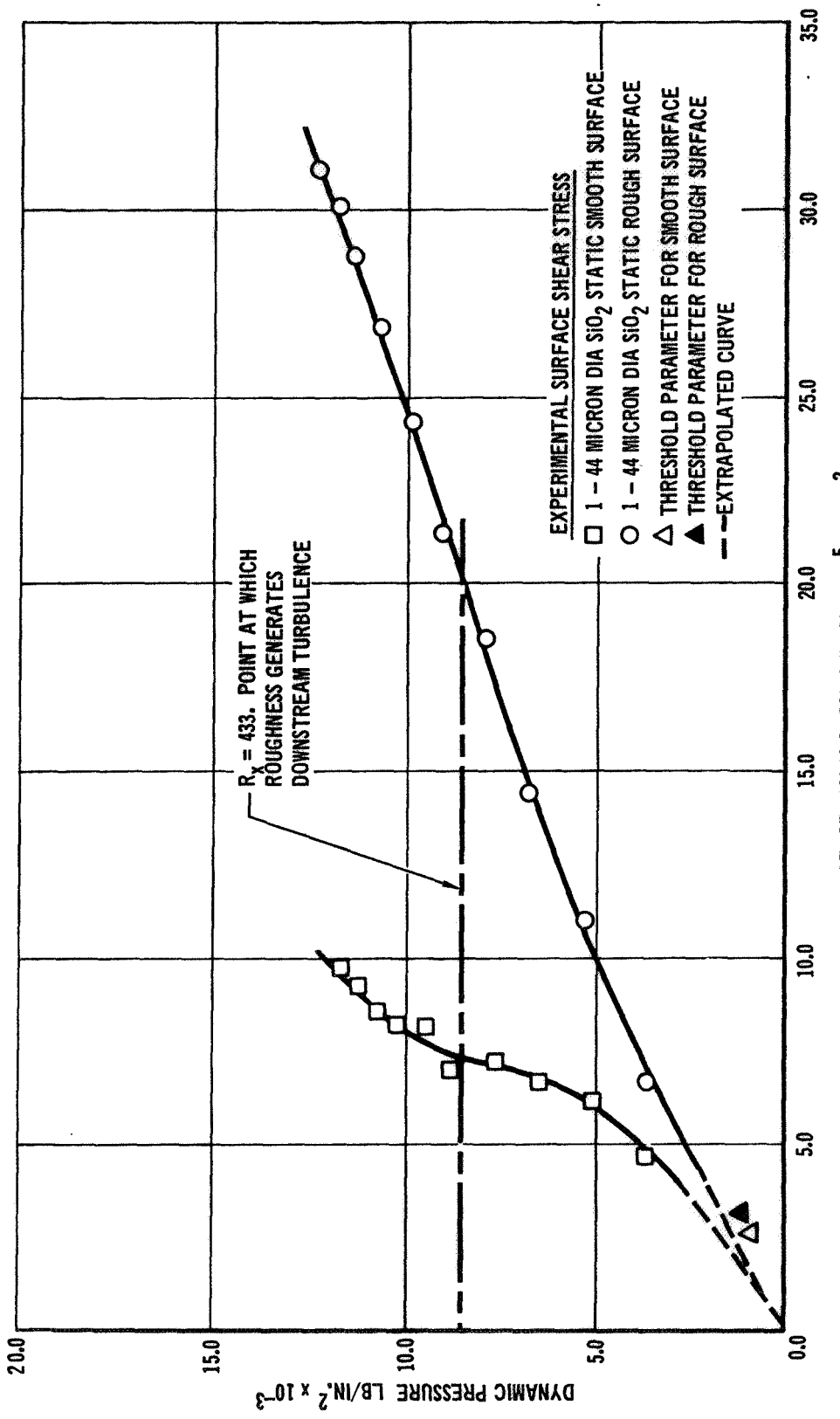

FIGURE 12 AERODYNAMIC SHEAR STRESS – 1 TO 44 MICRON DIA SiO_2

stress exerted on a surface and the particle size distribution on that surface was negated by the experimental error and/or is a functional mechanism affecting less than a 4.18×10^{-6} lb/in^2 change in the aerodynamic shear stress for the parameters investigated.

In addition, the aerodynamic shear stress exerted on a surface increases as the height of surface roughness increases for the parameters investigated. However, any quantitative analysis of this increase as a function of surface roughness is beyond the scope of this report.

4.1.2 BOUNDARY LAYER.

4.1.2.1 UNCOATED POLISHED PLATE. The boundary layer over the uncoated polished plate was not experimentally determined during the course of this investigation, so theoretical values were calculated using the Blasius boundary layer equations and are illustrated in Figure 13. The air flow parameters used in these calculations were arbitrarily selected from Figure 17 so that some comparison of the boundary layers of the uncoated polished plate and the 1 to 44 micron diameter smooth surface could be made.

4.1.2.2 SMOOTH AND ROUGH SURFACES. The boundary layers near the inception of surface erosion were determined for the eight surface models using the impact tube probe described in Section 3.2.1. They are graphically illustrated in Figures 14 through 21, and tabulated in Tables 3 through 10 so that the air flow surface interaction conditions are established. The data indicate that boundary layer thickness increases as the height of surface roughness increases for the parameters investigated. Any quantitative analysis of the functional relationship between boundary layer thickness and surface parameters is, again, beyond the scope of this report.

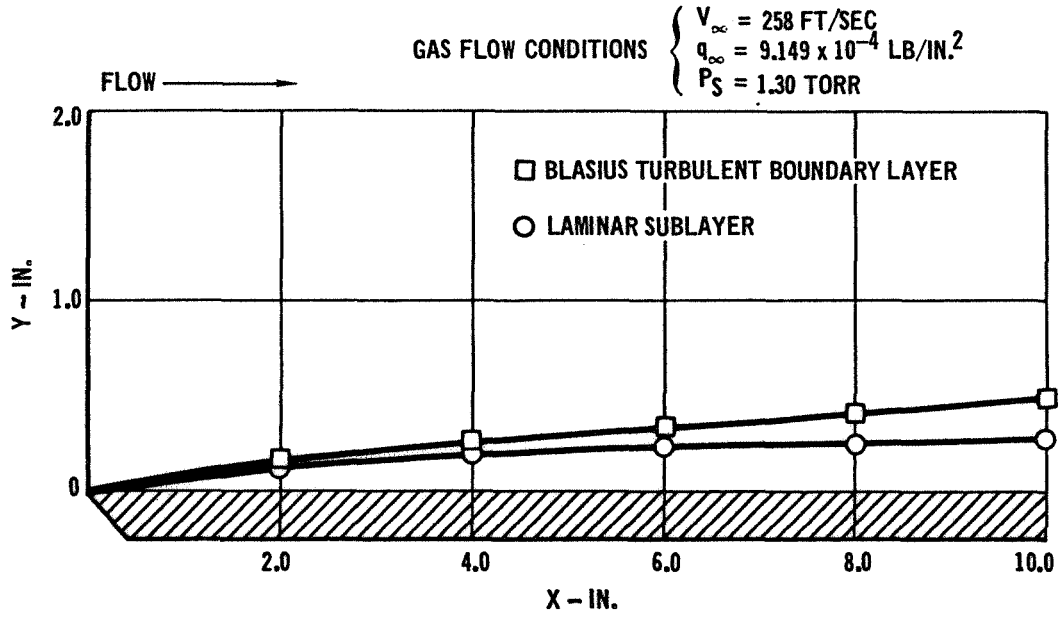

FIGURE 13 THEORETICAL BOUNDARY LAYER OVER UNCOATED POLISHED PLATE

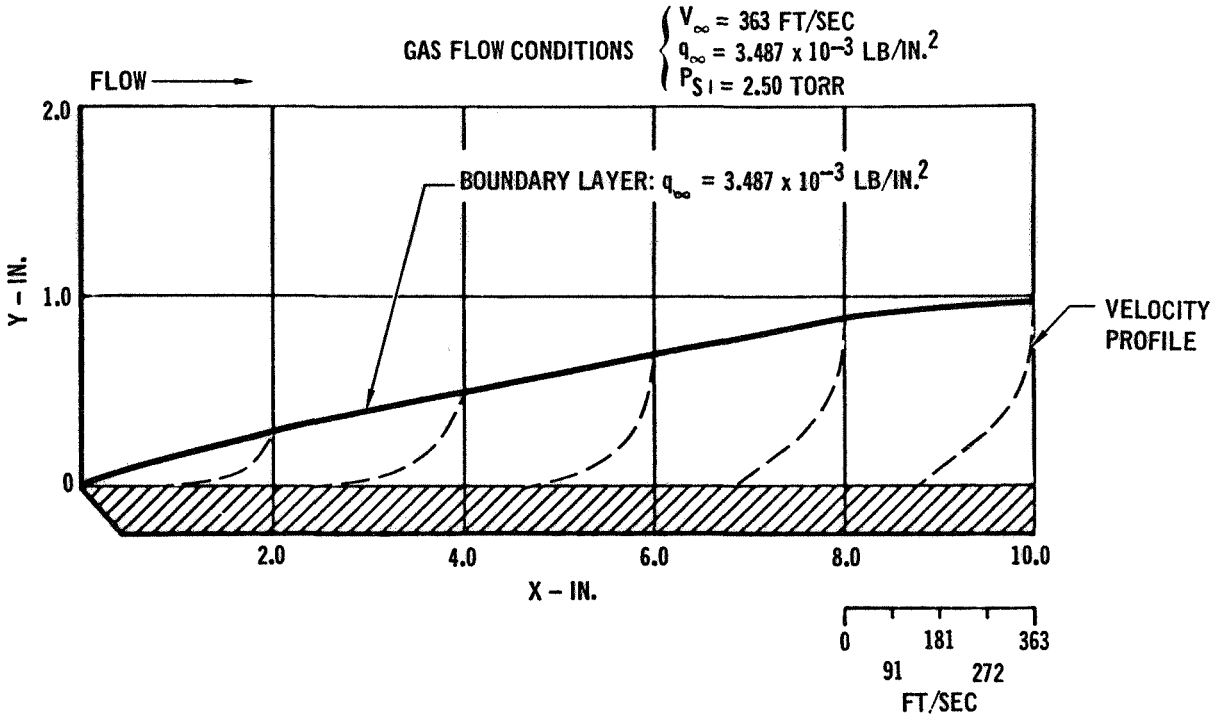

FIGURE 14 EXPERIMENTAL BOUNDARY LAYER OVER SMOOTH SURFACE OF 1 TO 500 MICRON DIA SiO_2 NEAR THRESHOLD CONDITIONS

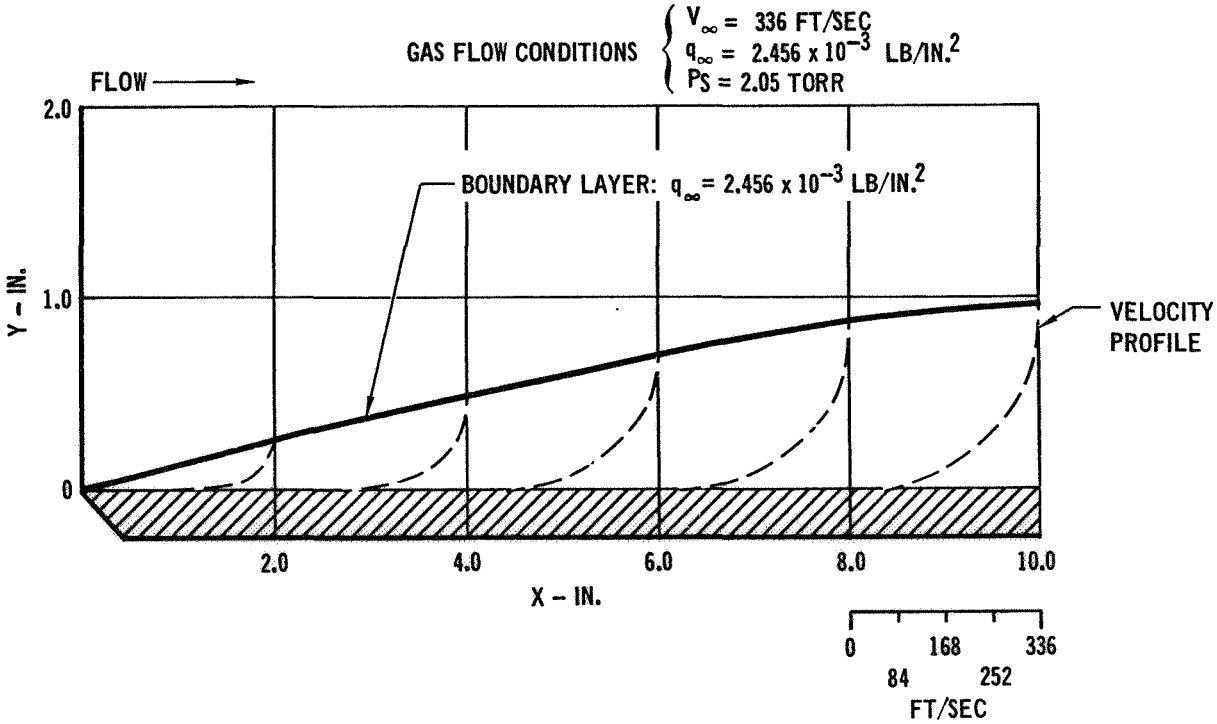

FIGURE 15 EXPERIMENTAL BOUNDARY LAYER OVER SMOOTH SURFACE OF 177 TO 210 MICRON DIA SiO_2 NEAR THRESHOLD CONDITIONS

TABLE 3 EXPERIMENTAL BOUNDARY LAYER DATA (REF FIGURE 14) SMOOTH SURFACE COATED WITH 1 TO 500 MICRON DIA SiO_2

GAS FLOW CONDITIONS { V_∞ 363 FT/SEC; q_∞ 3.487×10^{-3} LB/IN.^{2}; P_s 2.50 TORR

Y-IN.	X 0 IN.		X 2.0 IN.		X 4.0 IN.		X 6.0 IN.		X 8.0 IN.		X 10.0 IN.	
	V_∞ FT/SEC	q_∞ $\times 10^{-3}$ LB/IN.^{2}	V_∞ FT/SEC	q_∞ $\times 10^{-3}$ LB/IN.^{2}	V_∞ FT/SEC	q_∞ $\times 10^{-3}$ LB/IN.^{2}	V_∞ FT/SEC	q_∞ $\times 10^{-3}$ LB/IN.^{2}	V_∞ FT/SEC	q_∞ $\times 10^{-3}$ LB/IN.^{2}	V_∞ FT/SEC	q_∞ $\times 10^{-3}$ LB/IN.^{2}
0.062	358	3.401	187	0.9227	153	0.6176	153	0.6176	135	0.4830	121	0.3873
0.25	358	3.401	353	3.305	326	2.807	322	2.523	247	1.624	253	1.695
0.50	363	3.487	363	3.487	363	3.487	358	3.401	347	3.192	348	3.210
1.00	363	3.487	363	3.487	363	3.487	363	3.487	363	3.487	363	3.487
2.00	363	3.487	363	3.487	363	3.487	363	3.487	363	3.487	363	3.487

TABLE 4 EXPERIMENTAL BOUNDARY LAYER DATA (REF FIGURE 15) SMOOTH SURFACE COATED WITH 177 TO 210 MICRON DIA SiO_2

GAS FLOW CONDITIONS { V_∞ = 336 FT/SEC; q_∞ = 2.456×10^{-3} LB/IN.^{2}; P_s = 2.05 TORR

Y-IN.	X = 0 IN.		X = 2.0 IN.		X = 4.0 IN.		X = 6.0 IN.		X = 8.0 IN.		X = 10.0 IN.	
	V_∞ FT/SEC	q_∞ $\times 10^{-3}$ LB/IN.^{2}	V_∞ FT/SEC	q_∞ $\times 10^{-3}$ LB/IN.^{2}	V_∞ FT/SEC	q_∞ $\times 10^{-3}$ LB/IN.^{2}	V_∞ FT/SEC	q_∞ $\times 10^{-3}$ LB/IN.^{2}	V_∞ FT/SEC	q_∞ $\times 10^{-3}$ LB/IN.^{2}	V_∞ FT/SEC	q_∞ $\times 10^{-3}$ LB/IN.^{2}
0.062	327	2.327	176	0.6756	149	0.4837	149	0.4837	133	0.3865	133	0.3865
0.25	336	2.456	328	2.346	323	2.270	268	1.561	248	1.337	210	0.9603
0.50	336	2.456	336	2.456	336	2.456	330	2.366	323	2.270	317	2.184
1.00	336	2.456	336	2.456	336	2.456	336	2.456	336	2.456	336	2.456
2.00	336	2.456	336	2.456	336	2.456	336	2.456	336	2.456	336	2.456

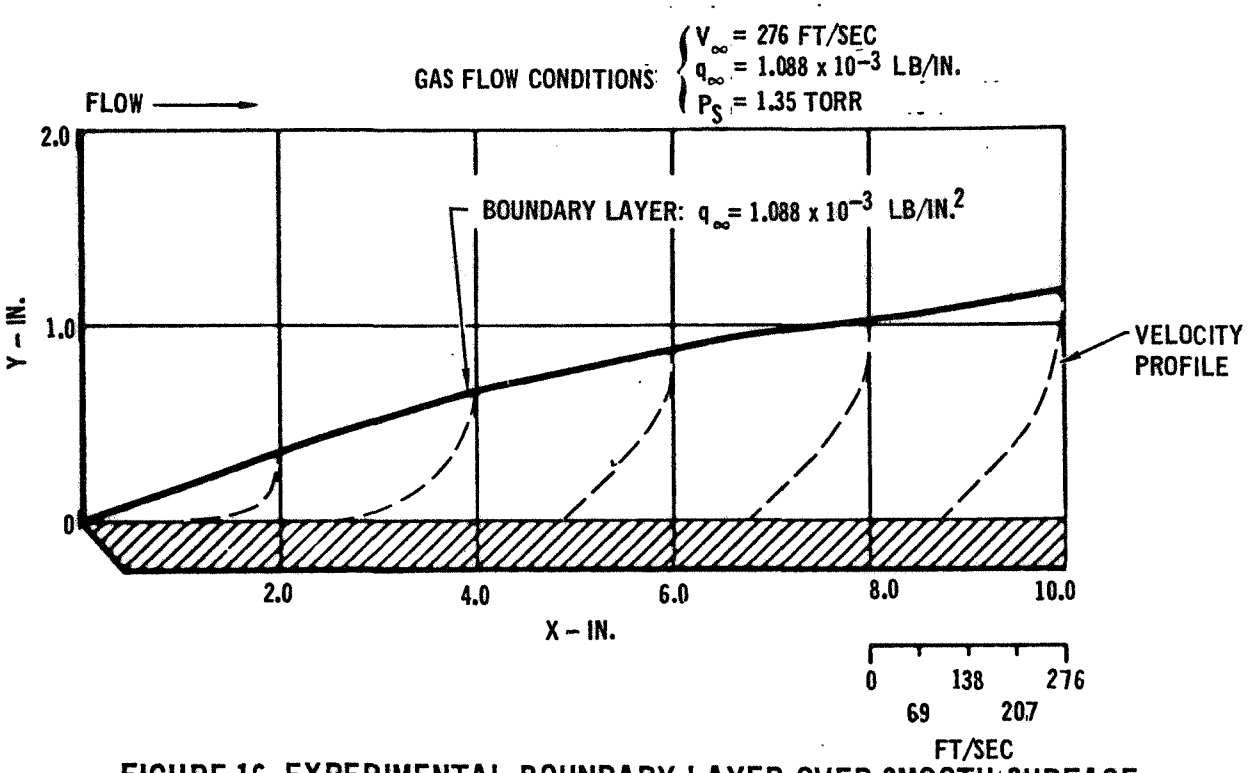

FIGURE 16 EXPERIMENTAL BOUNDARY LAYER OVER SMOOTH SURFACE OF 53 TO 63 MICRON DIA SiO_2 NEAR THRESHOLD CONDITIONS

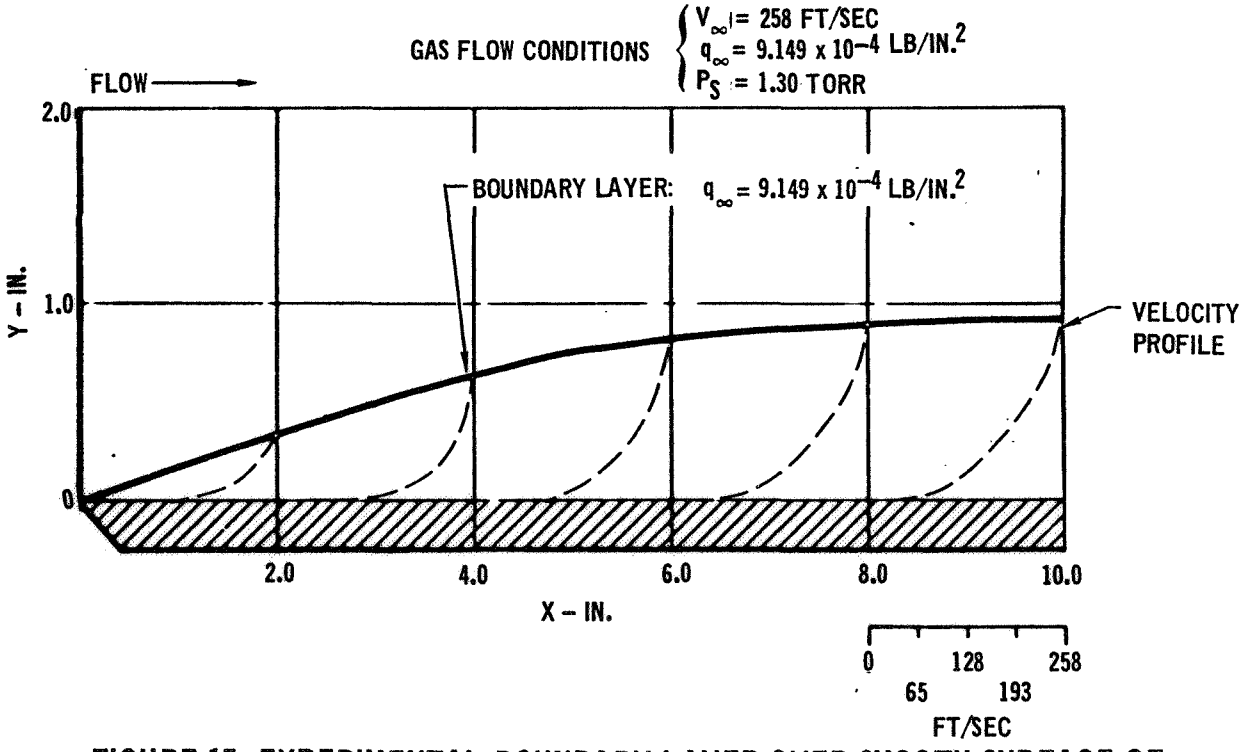

FIGURE 17 EXPERIMENTAL BOUNDARY LAYER OVER SMOOTH SURFACE OF 1 TO 44 MICRON DIA SiO_2 NEAR THRESHOLD CONDITIONS

TABLE 5 EXPERIMENTAL BOUNDARY LAYER DATA (REF FIGURE 16) SMOOTH SURFACE COATED WITH 53 TO 63 MICRON DIA SiO_2

GAS FLOW CONDITIONS $\begin{cases} V_\infty = 276 \text{ FT/SEC} \\ q_\infty = 1.088 \times 10^{-3} \text{ LB/IN.}^2 \\ P_S = 1.35 \text{ TORR} \end{cases}$

	X = 0 IN.		X = 2.0 IN.		X = 4.0 IN.		X = 6.0 IN.		X = 8.0 IN.		X = 10.0 IN.	
Y-IN.	V_∞ FT/SEC	q_∞ x 10^{-3} LB/IN.^{2}	V_∞ FT/SEC	q_∞ x 10^{-3} LB/IN.^{2}	V_∞ FT/SEC	q_∞ x 10^{-3} LB/IN.^{2}	V_∞ FT/SEC	q_∞ x 10^{-3} LB/IN.^{2}	V_∞ FT/SEC	q_∞ x 10^{-3} LB/IN.^{2}	V_∞ FT/SEC	q_∞ x 10^{-3} LB/IN.^{2}
0.062	276	1.088	127	0.2313	104	0.1546	104	0.1546	97	0.1352	94	0.1258
0.25	276	1.088	271	1.048	228	0.7417	188	0.5041	181	0.4691	172	0.4226
0.50	276	1.088	276	1.088	262	0.9785	261	0.9710	241	0.8292	238	0.8060
1.00	276	1.088	276	1.088	276	1.088	276	1.088	276	1.088	274	1.066
2.00	276	1.088	276	1.088	276	1.088	276	1.088	276	1.088	276	1.088

TABLE 6 EXPERIMENTAL BOUNDARY LAYER DATA (REF FIGURE 17) SMOOTH SURFACE COATED WITH 1 TO 44 MICRON DIA SiO_2

GAS FLOW CONDITIONS $\begin{cases} V_\infty = 258 \text{ FT/SEC} \\ q_\infty = 9.149 \times 10^{-4} \text{ LB/IN.}^2 \\ P_S = 1.30 \text{ TORR} \end{cases}$

	X = 0 IN.		X = 2.0 IN.		X = 4.0 IN.		X = 6.0 IN.		X = 8.0 IN.		X = 10.0 IN.	
Y-IN.	V_∞ FT/SEC	q_∞ x 10^{-3} LB/IN.^{2}	V_∞ FT/SEC	q_∞ x 10^{-3} LB/IN.^{2}	V_∞ FT/SEC	q_∞ x 10^{-3} LB/IN.^{2}	V_∞ FT/SEC	q_∞ x 10^{-3} LB/IN.^{2}	V_∞ FT/SEC	q_∞ x 10^{-3} LB/IN.^{2}	V_∞ FT/SEC	q_∞ x 10^{-3} LB/IN.^{2}
0.062	258	0.9149	114	0.1811	107	0.1569	101	0.1400	92	0.1154	84	0.0963
0.25	258	0.9149	245	0.8249	230	0.7267	195	0.5302	175	0.4229	140	0.2705
0.50	258	0.9149	258	0.9149	251	0.8672	240	0.7945	227	0.7110	212	0.6155
1.00	258	0.9149	258	0.9149	258	0.9149	258	0.9149	258	0.9149	258	0.9149
2.00	258	0.9149	258	0.9149	258	0.9149	258	0.9149	258	0.9149	258	0.9149

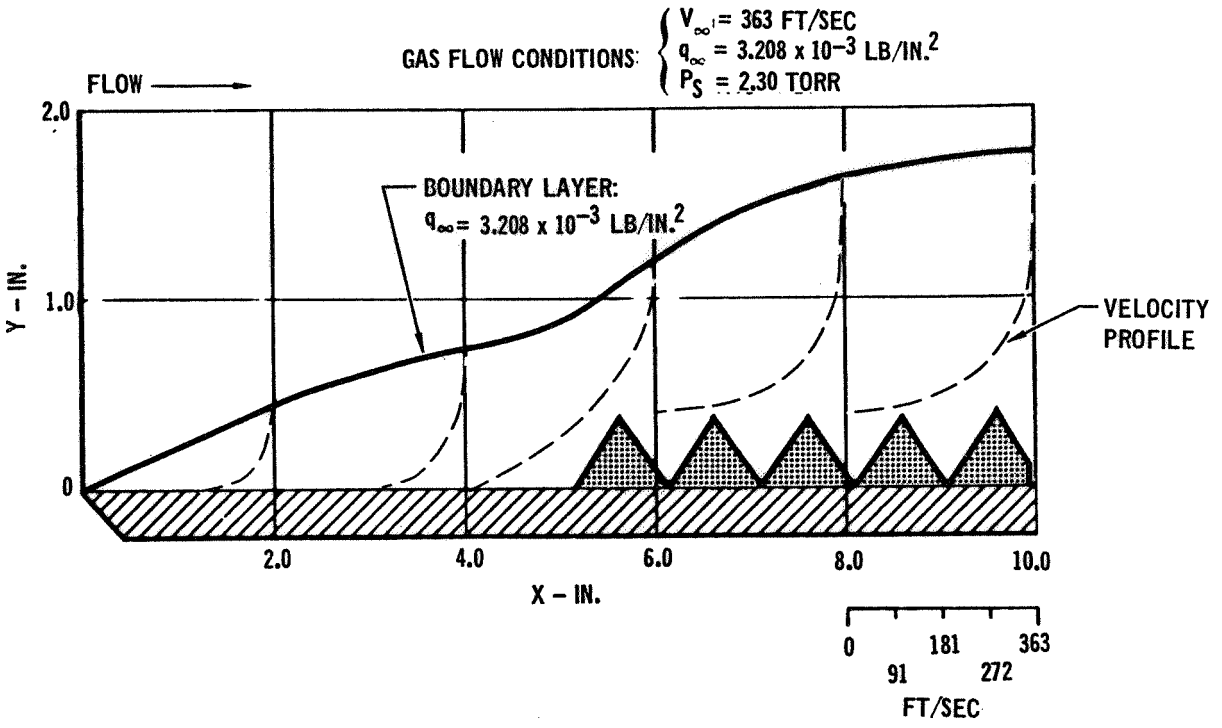

FIGURE 18 EXPERIMENTAL BOUNDARY LAYER OVER ROUGH SURFACE OF 1 TO 500 MICRON DIA SiO_2 NEAR THRESHOLD CONDITIONS

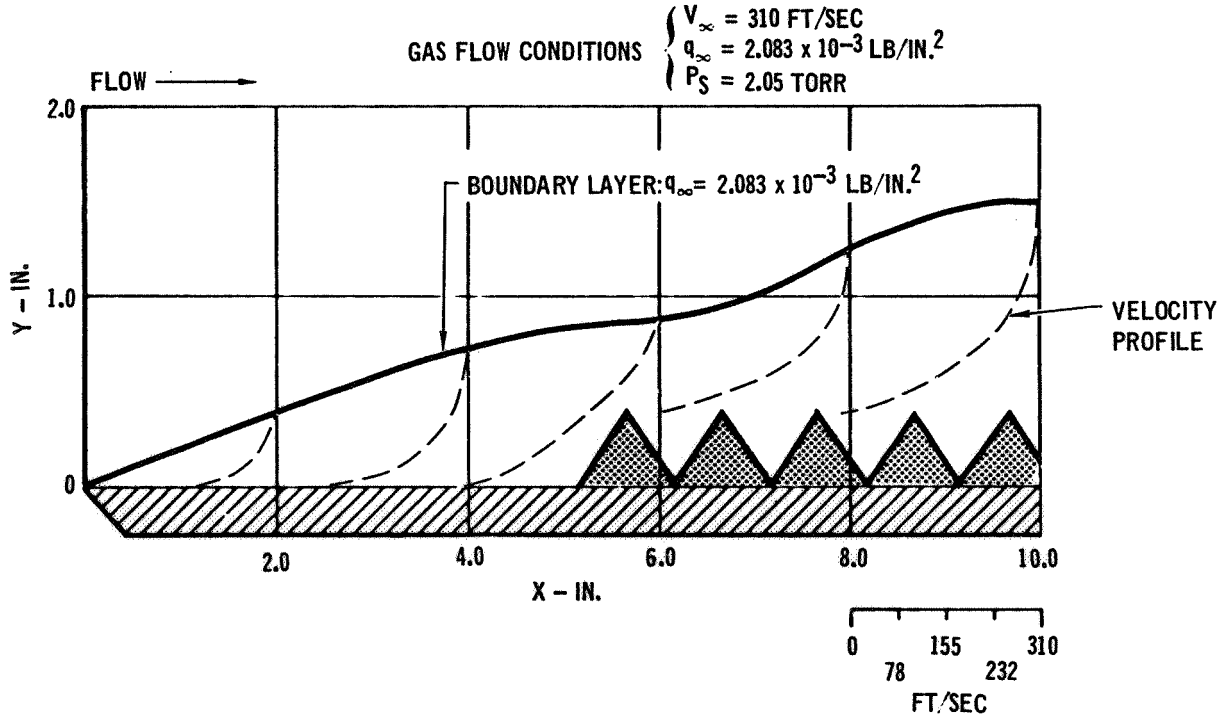

FIGURE 19 EXPERIMENTAL BOUNDARY LAYER OVER ROUGH SURFACE OF 177 TO 210 MICRON DIA SiO_2 NEAR THRESHOLD CONDITIONS

TABLE 7 EXPERIMENTAL BOUNDARY LAYER DATA (REF FIGURE 18) ROUGH SURFACE COATED WITH 1 TO 500 MICRON DIA SiO_2

GAS FLOW CONDITIONS { V_∞ - 363 FT/SEC; q_∞ - 3.208×10^{-3} LB/IN.^{2}; P_s - 2.30 TORR }

Y-IN.	X - 0 IN.		X - 2.0 IN.		X - 4.0 IN.		X - 6.0 IN.		X - 8.0 IN.		X - 10.0 IN.	
	V_∞ FT/SEC	q_∞ x 10^{-3} LB/IN.^{2}	V_∞ FT/SEC	q_∞ x 10^{-3} LB/IN.^{2}	V_∞ FT/SEC	q_∞ x 10^{-3} LB/IN.^{2}	V_∞ FT/SEC	q_∞ x 10^{-3} LB/IN.^{2}	V_∞ FT/SEC	q_∞ x 10^{-3} LB/IN.^{2}	V_∞ FT/SEC	q_∞ x 10^{-3} LB/IN.^{2}
0.25	363	3.208	352	3.021	327	2.610	←	*	→			
0.375	←	*	→									
0.50	363	3.208	363	3.208	357	3.109	262	1.680	213	1.109	198	0.5744
1.00	363	3.208	363	3.208	363	3.208	357	3.109	357	3.109	352	3.021
2.00	363	3.208	363	3.208	363	3.208	363	3.208	363	3.208	363	3.208

*NOT MEASURED

TABLE 8 EXPERIMENTAL BOUNDARY LAYER DATA (REF FIGURE 19) ROUGH SURFACE COATED WITH 177 TO 210 MICRON DIA SiO_2

GAS FLOW CONDITIONS { V_∞ = 310 FT/SEC; q_∞ 2.083 x 10^{-3} LB/IN.^{2}; P_s = 2.05 TORR }

Y-IN.	X = 0 IN.		X = 2.0 IN.		X = 4.0 IN.		X = 6.0 IN.		X = 8.0 IN.		X = 10.0 IN.	
	V_∞ FT/SEC	q_∞ x 10^{-3} LB/IN.^{2}	V_∞ FT/SEC	q_∞ x 10^{-3} LB/IN.^{2}	V_∞ FT/SEC	q_∞ x 10^{-3} LB/IN.^{2}	V_∞ FT/SEC	q_∞ x 10^{-3} LB/IN.^{2}	V_∞ FT/SEC	q_∞ x 10^{-3} LB/IN.^{2}	V_∞ FT/SEC	q_∞ x 10^{-3} LB/IN.^{2}
0.25	310	2.083	288	1.805	245	1.299	←	*	→			
0.375	←	*	→									
0.50	310	2.083	310	1.805	303	1.993	232	1.168	94	0.1911	94	0.1911
1.00	310	2.083	310	2.083	310	2.083	310	2.083	303	1.993	281	1.713
2.00	310	2.083	310	2.083	310	2.083	310	2.083	310	2.083	310	2.083

*NOT MEASURED

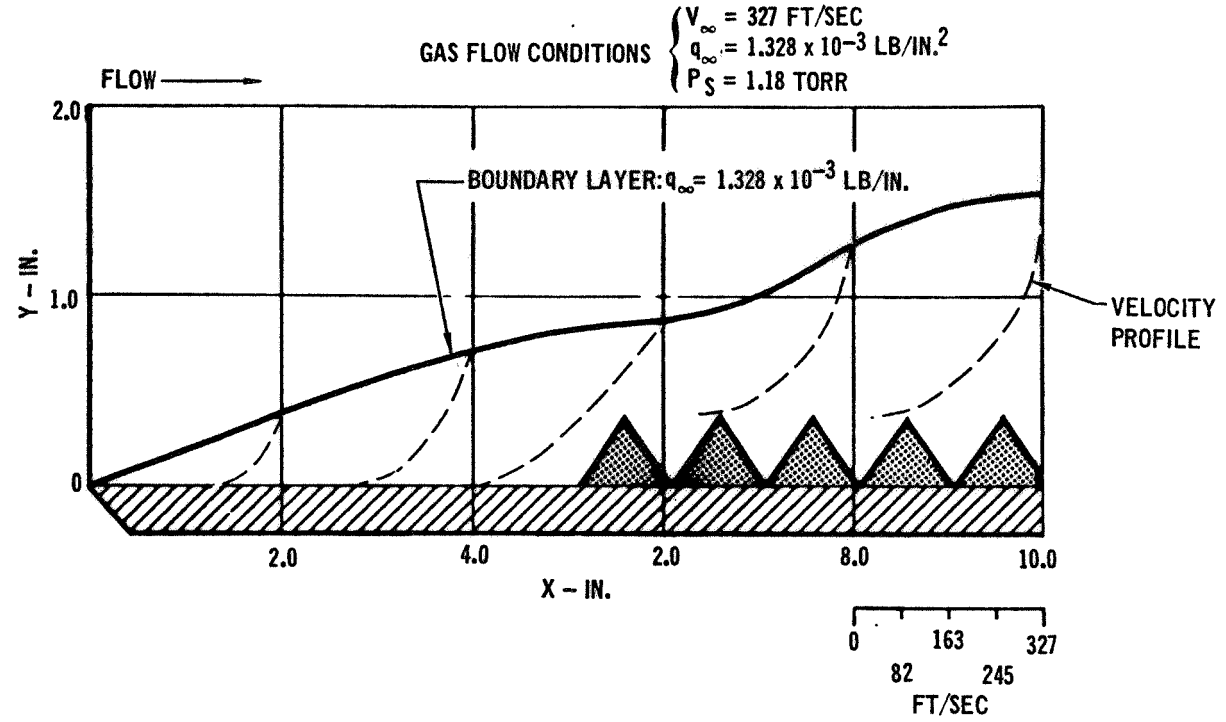

FIGURE 20 EXPERIMENTAL BOUNDARY LAYER OVER ROUGH SURFACE OF 53 TO 63 MICRON DIA SiO_2 NEAR THRESHOLD CONDITIONS

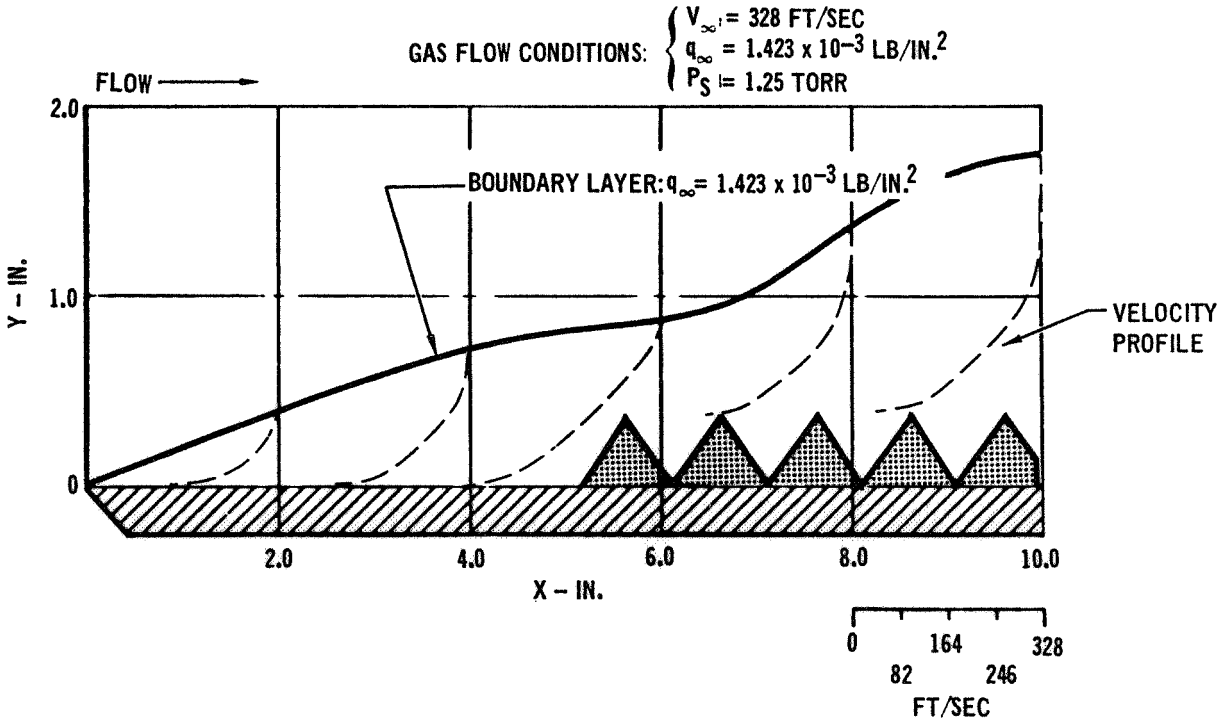

FIGURE 21 EXPERIMENTAL BOUNDARY LAYER OVER ROUGH SURFACE OF 1 TO 44 MICRON DIA SiO_2 NEAR THRESHOLD CONDITIONS

TABLE 9 EXPERIMENTAL BOUNDARY LAYER DATA (REF FIGURE 20) ROUGH SURFACE COATED WITH 53 TO 63 MICRON DIA SiO_2

GAS FLOW CONDITIONS $\begin{cases} V_\infty = 327 \text{ FT/SEC} \\ q_\infty = 1.328 \times 10^{-3} \text{ LB/IN.}^2 \\ P_s = 1.18 \text{ TORR} \end{cases}$

	X = 0 IN.		X = 2.0 IN.		X = 4.0 IN.		X = 6.0 IN.		X = 8.0 IN.		X = 10.0 IN.	
Y–IN.	V_∞ FT/SEC	q_∞ x 10^{-3} LB/IN.^{2}	V_∞ FT/SEC	q_∞ x 10^{-3} LB/IN.^{2}	V_∞ FT/SEC	q_∞ x 10^{-3} LB/IN.^{2}	V_∞ FT/SEC	q_∞ x 10^{-3} LB/IN.^{2}	V_∞ FT/SEC	q_∞ x 10^{-3} LB/IN.^{2}	V_∞ FT/SEC	q_∞ x 10^{-3} LB/IN.^{2}
0.25	327	1.328	315	1.234	251	0.7814	*		*			
0.375	*		*		*		171	0.3658	114	0.1631	96	0.1155
0.50	327	1.328	327	1.328	306	1.163	225	0.6307	184	0.4237	136	0.2314
1.00	327	1.328	327	1.328	327	1.328	327	1.328	306	1.163	298	1.103
2.00	327	1.328	327	1.328	327	1.328	327	1.328	327	1.328	327	1.328

*NOT MEASURED

TABLE 10 EXPERIMENTAL BOUNDARY LAYER DATA (REF FIGURE 21) ROUGH SURFACE COATED WITH 1 TO 44 MICRON DIA SiO_2

GAS FLOW CONDITIONS $\begin{cases} V_\infty = 328 \text{ FT/SEC} \\ q_\infty = 1.423 \times 10^{-3} \text{ LB/IN.}^2 \\ P_s = 1.25 \text{ TORR} \end{cases}$

	X = 0 IN.		X = 2.0 IN		X = 4.0 IN.		X = 6.0 IN.		X = 8.0 IN.		X = 10.0 IN.	
Y–IN.	V_∞ FT/SEC	q_∞ x 10^{-3} LB/IN.^{2}	V_∞ FT/SEC	q_∞ x 10^{-3} LB/IN.^{2}	V_∞ FT/SEC	q_∞ x 10^{-3} LB/IN.^{2}	V_∞ FT/SEC	q_∞ x 10^{-3} LB/IN.^{2}	V_∞ FT/SEC	q_∞ x 10^{-3} LB/IN.^{2}	V_∞ FT/SEC	q_∞ x 10^{-3} LB/IN.^{2}
0.25	328	1.423	312	1.289	254	0.8583	*		*			
0.375	*		*		*		171	0.3858	121	0.1936	107	0.1547
0.50	328	1.423	328	1.423	317	1.327	249	0.8211	198	0.5183	161	0.3468
1.00	328	1.423	328	1.423	328	1.423	328	1.423	317	1.327	298	1.180
2.00	328	1.423	328	1.423	328	1.423	328	1.423	327	1.423	328	1.423

*NOT MEASURED

4.2 SURFACE EROSION.

4.2.1 SURFACE SHEAR STRESS. The maximum surface resistivity to erosion, or threshold surface shear stress, of the surfaces in relation to the aerodynamic shear stress is given in Figures 9 through 12. Theoretically, at threshold conditions, the aerodynamic shear stress on a surface should just exceed the maximum resistivity to erosion of that surface. The threshold data for the respective particle size distributions, for both surface profiles, illustrates that the surface resistivity was either equal to or greater than the aerodynamic shear stress. This apparent contradiction, however, is again seen to be within the probable experimental error and may be explained accordingly.

The threshold surface shear stress or resistivity of the surfaces is compiled with other surface erosion parameters in Table 11. It decreases as particle size decreases for both surface profiles except for the smooth surface of 1 to 44 micron diameter particles. This deviation or increase in resistivity of the 1 to 44 micron smooth surface may be the result of increased particle cohesion and/or adhesion, or surface compaction induced during the "raking" phase of surface model preparation. Disregarding this particular discrepancy, it may be concluded that the surface threshold shear stress decreases as surface particle size distribution decreases for the parameters investigated.

The data in Table 11 also illustrate that the threshold surface shear stress, or resistivity for each particle size group, is greater for the rough surface profiles than for the smooth, except for the size distribution of particles ranging from 177 to 210 microns in diameter. This increase in surface resistivity, except for the 177 to 210 micron diameter surface, is again believed to be a result of surface compaction rather than surface roughness. If so, any relation between threshold surface shear stress and surface profile or roughness was

TABLE 11 EXPERIMENTAL DATA – THRESHOLD PARAMETERS

DYNAMIC SURFACE PROFILE	SURFACE PARTICLE SIZE DISTRIBUTION (MICRONS)	STATIC PRESSURE (TORR)	GAS VELOCITY (FT/SEC)	GAS FLOW DYNAMIC PRESSURE ($LB/IN.^2$)	SURFACE SHEAR STRESS ($LB/IN.^2$)	PARTICLE DEPARTURE VELOCITY (FT/SEC)	PARTICLE DEPARTURE ANGLE
SMOOTH	1–500	2.52	356	3.40×10^{-3}	5.50×10^{-5}	1–5.50	20^0–80^0
	177–210	2.09	318	2.27	3.95	1–5.50	20^0–80^0
	53–63	1.35	275	1.08	2.35	–	–
	1–44	1.27	264	0.94×10^{-3}	2.70×10^{-5}	–	–
ROUGH	1–500	2.25	373	3.32×10^{-3}	6.05×10^{-5}	1–5.50	40^0–130^0
	177–210	2.00	307	1.99	3.89	1–5.50	40^0–130^0
	53–63	1.15	333	1.34	3.37	–	–
	1–44	1.18	313	1.20×10^{-3}	3.16×10^{-5}	–	–

negated by surface compaction for the parameters investigated.

4.2.2 PARTICLE MOTION. Photographs showing incipient erosion are given in Figures 22 through 26. Analyses of these and similar photographs for both surface profiles determined that the threshold particle velocities range from 1 to 5.50 ft/sec, with an average of 2.20 ft/sec, for the 1 to 500 micron particle size distribution; and from 1 to 5.50 ft/sec, with an average of 2.24 ft/sec, for the 177 to 210 micron particle size distribution. The difference between the average values is within the probable experimental error, so the data may indicate that the threshold particle velocity is not affected by surface particle size distribution, and ranges from 1 to 5.50 ft/sec for the parameters investigated.

Analyses of these photographs for both 1 to 500 micron and 177 to 210 micron particle size distributions also determined that the threshold particle velocities range from 1 to 5.50 ft/sec, with an average of 2.43 ft/sec, for the smooth surface profile; and from 1 to 5.50 ft/sec, with an average of 210 ft/sec, for the rough surface profile. The difference between the average values is, again within the probable experimental error, so the data may also indicate that the threshold particle velocity is not affected by the surface profile, and also ranges from 1 to 5.50 ft/sec for the parameters investigated.

No velocity data were obtained for the two lower size distributions because of the limits of the photographic system. However, it is believed that their initial particle velocity also is not affected by the surface particle size distribution or surface profile.

In addition to the above, analyses of these photographs for both surface profiles determined that the threshold particle departure angles range from 20 to 130 degrees, with an average of 73 degrees, for the 1 to 500 micron

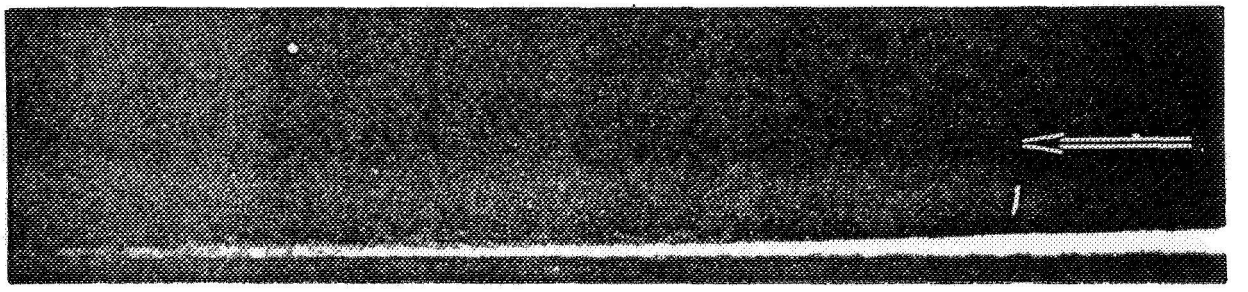

FIGURE 22 1 TO 500 MICRON DIA SiO_2 SMOOTH SURFACE AT THRESHOLD CONDITIONS. $q_\infty = 3.40 \times 10^{-3}$ LB/IN^2

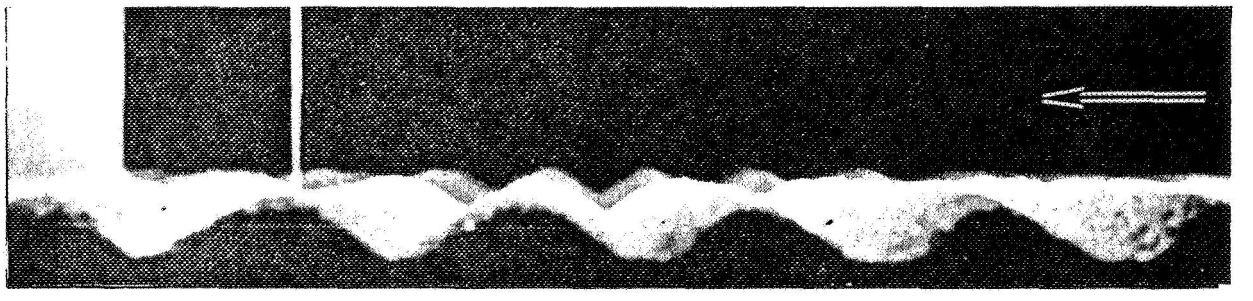

FIGURE 23 1 TO 500 MICRON DIA SiO_2 ROUGH SURFACE AT THRESHOLD CONDITIONS. $q_\infty = 3.32 \times 10^{-3}$ LB/IN^2

FIGURE 24 177 TO 210 MICRON DIA SiO_2 ROUGH SURFACE AT THRESHOLD CONDITIONS. $q_\infty = 1.99 \times 10^{-3}$ LB/IN^2

FIGURE 25 53 TO 63 MICRON DIA SiO_2 SMOOTH SURFACE AT THRESHOLD CONDITIONS. $q_\infty = 1.08 \times 10^{-3}$ LB/IN.^{2}

FIGURE 26 53 TO 63 MICRON DIA SiO_2 ROUGH SURFACE AT THRESHOLD CONDITIONS. $q_\infty = 1.34 \times 10^{-3}$ LB/IN.^{2}

particle size distribution; and from 20 to 130 degrees, with an average of 52 degrees, for the 177 to 210 micron particle size distribution. In other words, the threshold particle departure angle decreases as particle size decreases for the parameters investigated.

Furthermore, analyses of these plates, for both the 1 to 500 micron particle size distribution and the 177 to 210 micron particle size distribution, also determined that the threshold particle departure angles range from 20 to 80 degrees, with an average of 50 degrees, for the smooth surface profile; and from 40 to 130 degrees, with an average of 78 degrees, for the rough surface profile. That is, the threshold particle departure angles increase as the height of surface roughness increases for the parameters investigated.

No entrainment angle data were obtained for the lower distributions because of the limits of the photographic system. However, it is believed that their threshold particle departure angles also decrease as particle size decreases, and increase as the height of surface roughness increases.

4.3 ENTRAINED PARTICLES. Saltation layer weight distributions are given in Figures 27 and 28. These data illustrate that the particle transport within 1 inch of the surface increases as particle size decreases for each surface profile, except for the smooth surface of 1 to 44 micron diameter particles. However, if surface compaction is considered as discussed in Section 4.2.1, these figures indicate that surface transport within 1 inch of an eroding surface increases as surface particle size distribution decreases for the parameters investigated.

Figures 27 and 28 also illustrate that the maximum saltation height for each particle size distribution decreases as the height of surface roughness increases for the parameters investigated, if surface compaction of the 1 to 44 micron in diameter particle surface is considered.

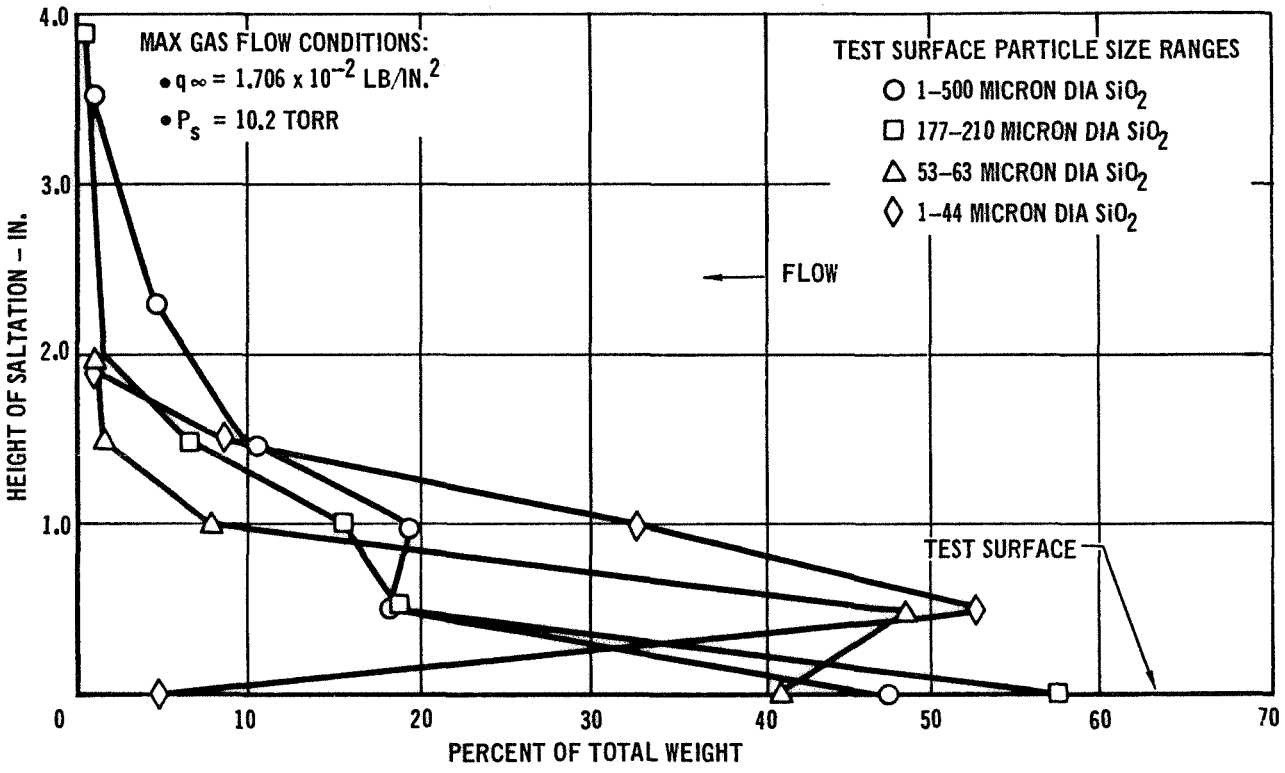

FIGURE 27 SALTATION WEIGHT DISTRIBUTION FOR A SMOOTH DYNAMIC SURFACE

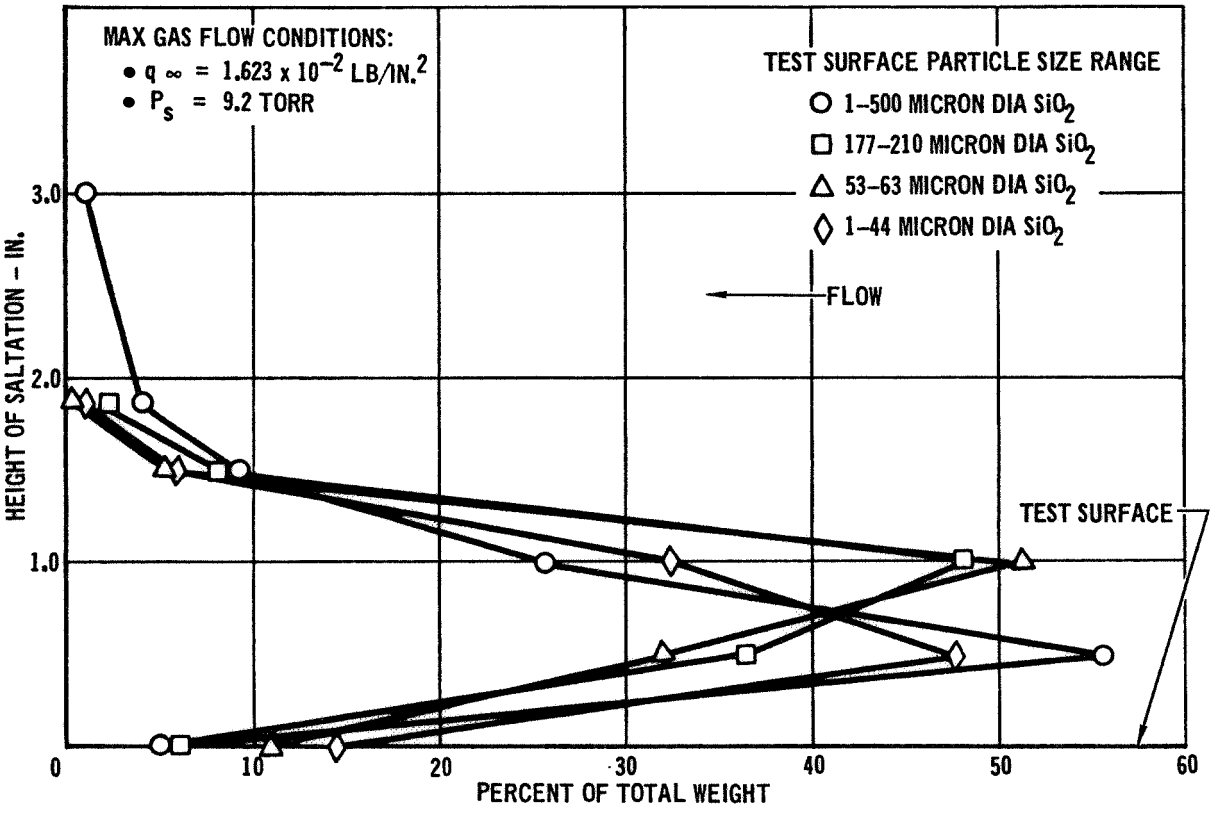

FIGURE 28 SALTATION WEIGHT DISTRIBUTION FOR A ROUGH DYNAMIC SURFACE

The saltation layer size distributions for the 1 to 500 micron diameter particle surface are given in Figures 29 and 30. These data indicate no apparent particle size selection in relation to height for both surface profiles.

Saltation layer size distributions were not determined for the other surface models because of the physical limitations of the photomicrographic technique used for analysis.

4.4 PARTICLE MATERIAL EFFECT. Three types of particulate material were studied during the initial phase of this investigation--aluminum oxide (Al_2O_3, sp. gr. 3.97), glass spheres, and silicon dioxide (SiO_2, sp. gr. 2.66).

The Al_2O_3 was chosen as the original surface particulate material because of its availability in the desired size distributions. During the course of events, it was noted that photographic analysis of the entrainment mechanism was not possible because the entrained particle tracks were indistinct. At this time, photographs were taken of entrained Al_2O_3 particles without the shutter disk rotating or, in other words, without the shutter disk interrupting the light reflected by entrained particles. These photographs showed that the particle tracks were not solid, as was expected without the shutter disk rotating, but were intermittent or broken. (See Figure 31.) Analysis of this phenomenon indicates that track intermittency is the result of light being reflected by different facets of a particle as it rotates in flight. As a result of this, the additional track interruption by the shutter disk rotating completely "washed out" any particle track. The Al_2O_3 was abandoned as the particulate material for this reason. Before it was abandoned, however, the threshold dynamic pressure and saltation layer weight distribution of a smooth surface of 1 to 500 micron diameter Al_2O_3 were determined. The threshold dynamic pressure is

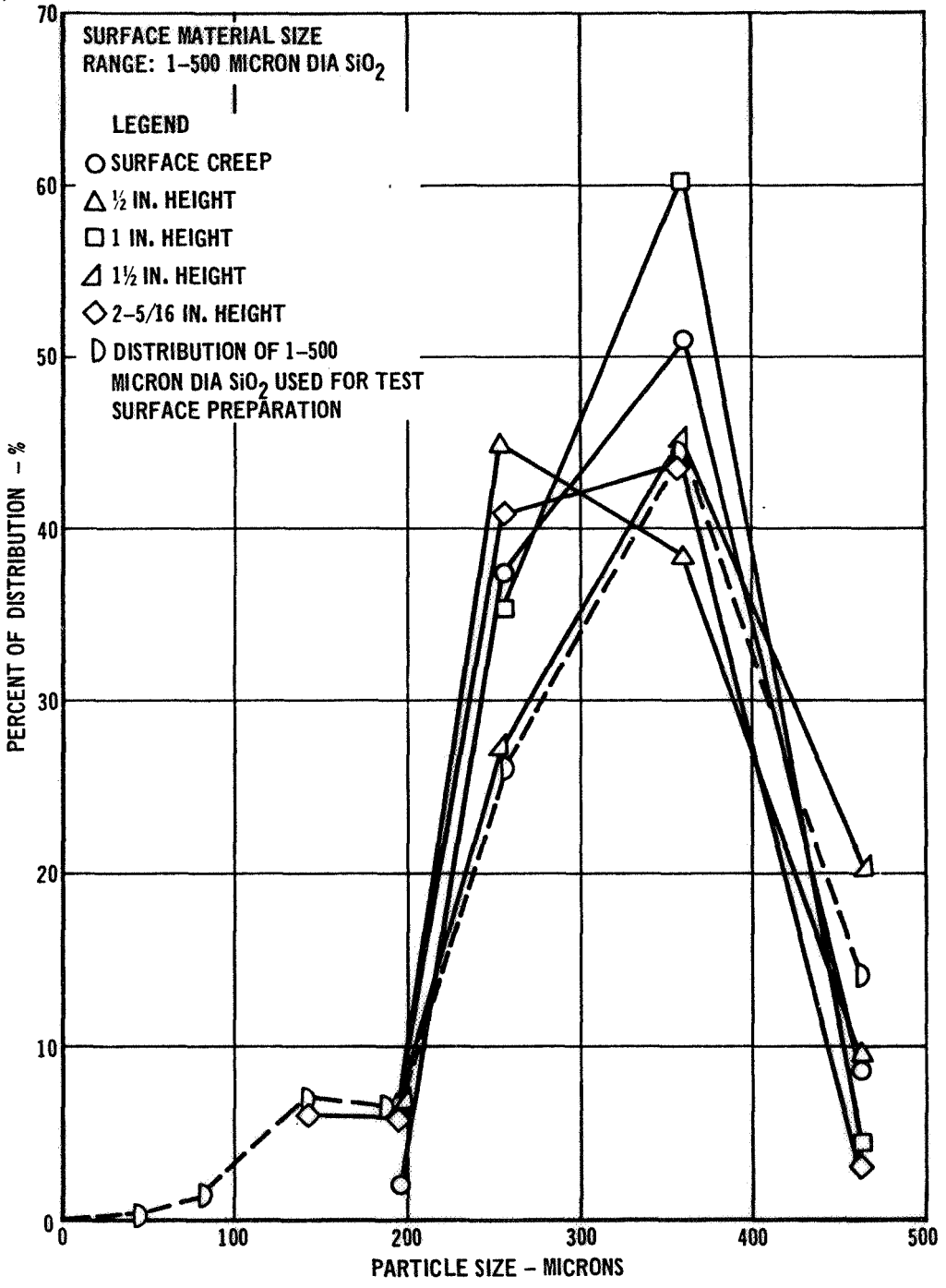

FIGURE 29 SALTATION PARTICLE SIZE DISTRIBUTION FOR A SMOOTH DYNAMIC SURFACE

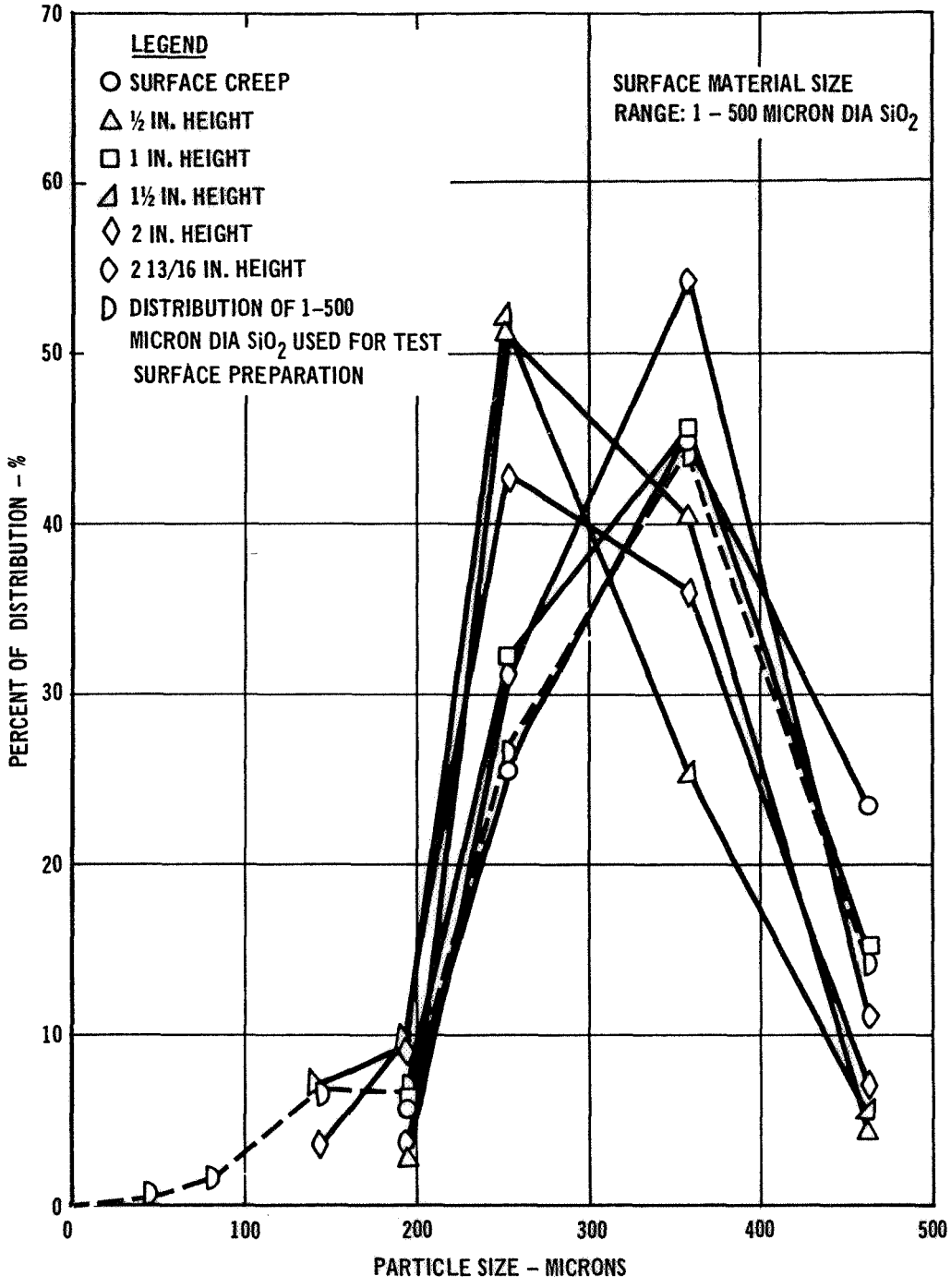

FIGURE 30 SALTATION PARTICLE SIZE DISTRIBUTION FOR A ROUGH DYNAMIC SURFACE

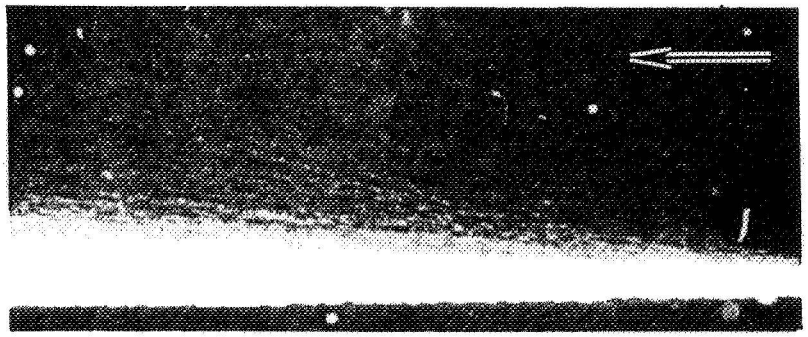

FIGURE 31 1 TO 500 MICRON DIA Al_2O_3 ROTATING DURING SALTATION

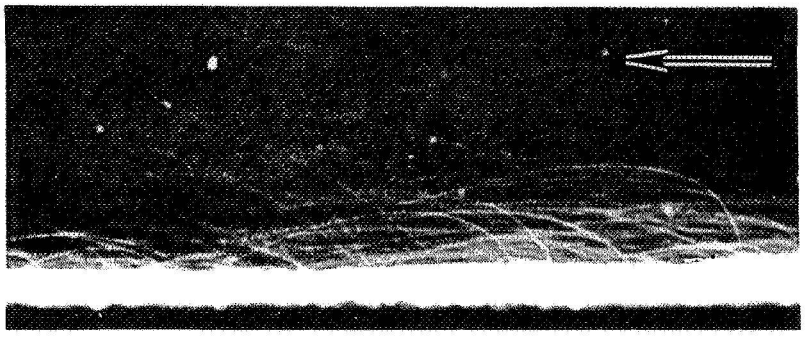

FIGURE 32 210 TO 420 MICRON DIA GLASS SPHERES ROTATING DURING SALTATION

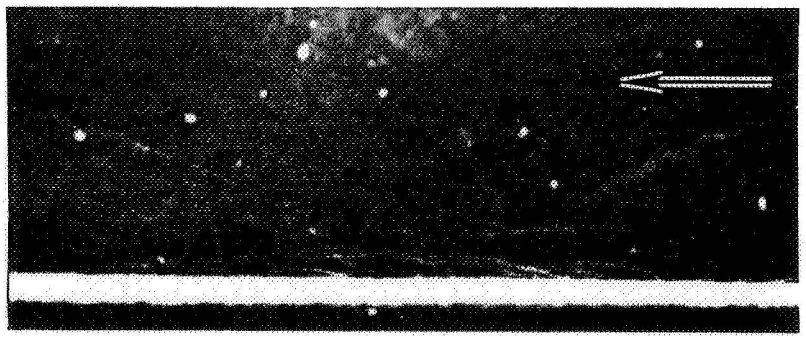

FIGURE 33 297 TO 420 MICRON DIA SiO_2 ROTATING DURING SALTATION.

1.02×10^{-2} lb/in^2 and the saltation layer weight distribution is given in Figure 34.

Comparison of the threshold dynamic pressures of the 1 to 500 micron diameter Al_2O_3 and SiO_2 indicates that the surface resistivity of the Al_2O_3 is greater than that of the SiO_2; and as a result, the threshold dynamic pressure for the Al_2O_3 is greater than that of the SiO_2. This can most easily be explained as the result of greater particle density and differing shape. (See Figures 35 and 36).

Comparison of the saltation layer weight distributions of the 1 to 500 micron diameter Al_2O_3 and SiO_2 (Figures 27 and 34) indicates that the Al_2O_3 transport is closer to the surface than the SiO_2. This, too, can be most easily be explained as the result of greater particle density and differing shape.

After the abandonment of Al_2O_3, glass spheres were studied for their optical properties. It was assumed that these particles would continuously reflect light because of their symmetry, even if rotating. Photographs of inflight particles showed this to be true except for isolated cases. (See Figure 32.) It is believed that these isolated intermittent particle tracks are the result of several particles adhering, thereby producing unsymmetrical surfaces.

Comparison of Figures 31 and 32 indicates the photographic advantage of glass spheres. However, they, too, were abandoned as the particulate material because rough surface profiles could not be constructed with them. In addition to this, their threshold dynamic pressure was found to be extremely low (lower than the dynamic pressure range defined in Section 3.2.2).

Finally, SiO_2 was studied for its optical properties. Photographs of inflight particles showed that rotation of these particles did not affect the reflected light as much as the Al_2O_3. (See Figure 33.) Based on the optical

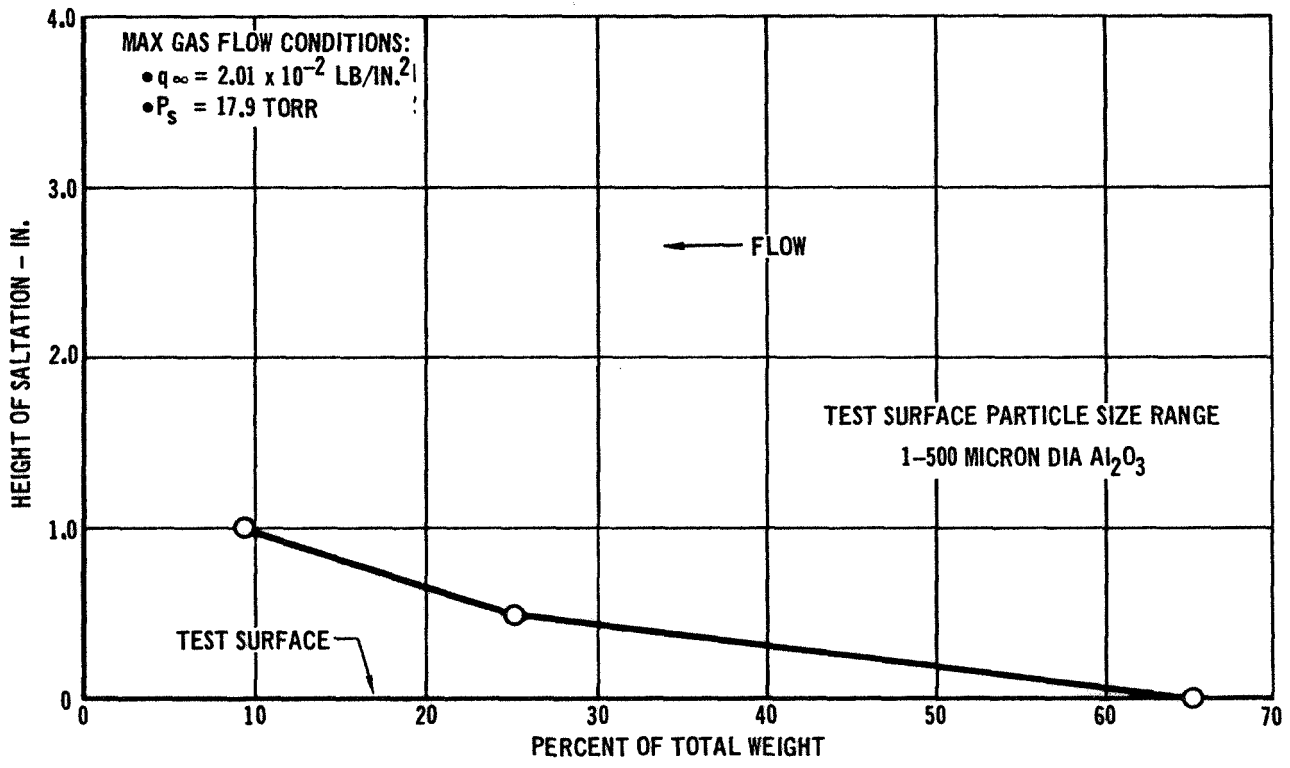

FIGURE 34 SALTATION WEIGHT DISTRIBUTION FOR A SMOOTH DYNAMIC SURFACE

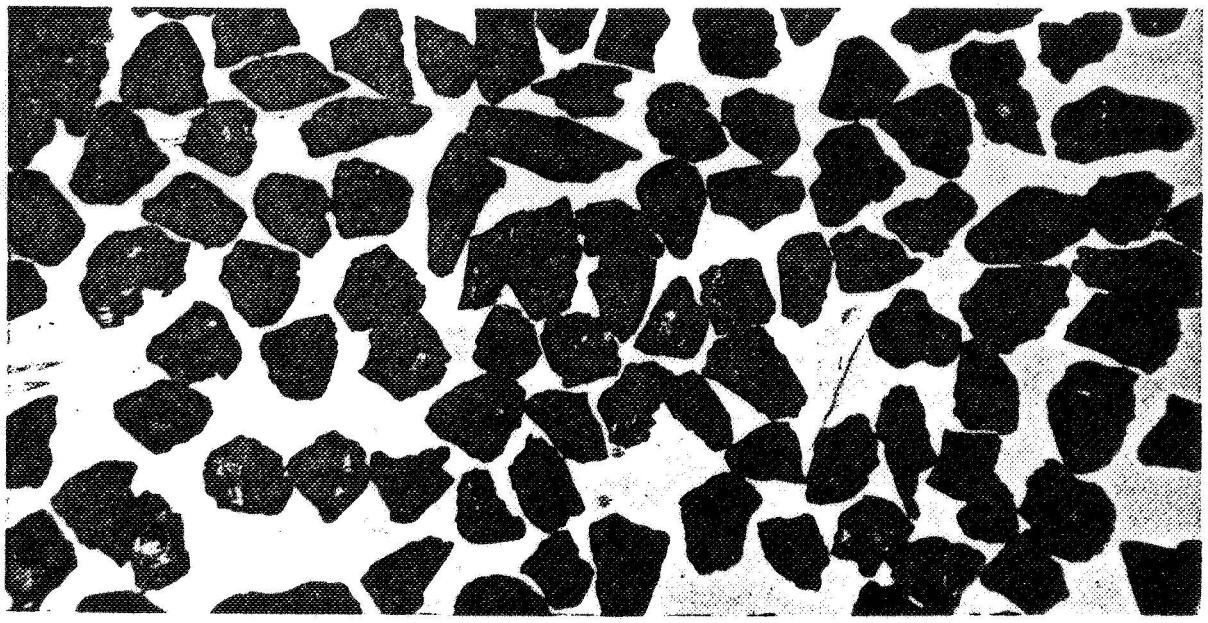

MAGNIFICATION 40X

FIGURE 35 PHOTOMICROGRAPH OF 177 TO 210 MICRON DIA Al_2O_3

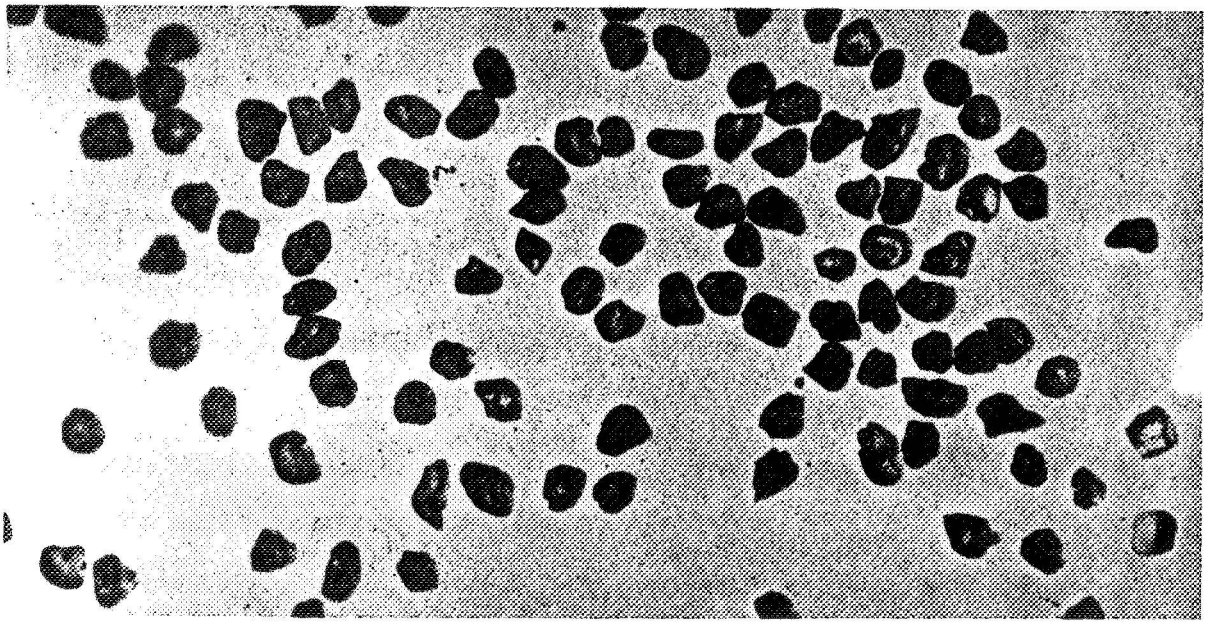

MAGNIFICATION 25X

FIGURE 36 PHOTOMICROGRAPH OF 177 TO 210 MICRON DIA SiO_2

advantage of SiO_2 and its similarity to the lunar material (Figure 5), it was chosen as the surface particulate material for this investigation.

4.5 CONCLUDING REMARKS. Observations made during this investigation are summarized below:

1. Experimentally measured values of aerodynamic shear stress on an uncoated polished plate agreed closely with theoretical values.

2. The measured aerodynamic shear stress on the test surface did not vary significantly or systematically with particle size in the range of sizes that were tested.

3. The measured aerodynamic shear stress on the test surface increased with surface roughness.

4. The airstream dynamic pressure required to initiate saltation and entrainment of particles increased with the average particle size.

5. The airstream velocities at the start of erosion are in the same order of magnitude as the wind velocities expected to be encountered on Mars. The test static pressures were approximately those expected on Mars.

6. Particles released from the surface by the saltation process were observed to leave over a large range of angles, including an upstream component of velocity. Particles were also observed to spin.

7. The size distribution of entrained particles did not vary systematically with height above the surface nor differ markedly from that of the surface particles.

8. Most of the entrained particles were within one inch of the surface.

9. Some brief tests showed that particles with a higher density required a higher airstream dynamic pressure to initiate erosion. It was also

observed that the denser particles did not rise as high when airborne as the lighter particles.

10. Spherical particles eroded at extremely low dynamic pressures from a smooth surface.

11. It is believed that surface compaction has a strong influence on the erosion boundary of fine particles.

12. An experimental technique was developed that provided useful data about the dislodgement of solid particles by a low density airstream flowing along a particulate surface, and the motion of these particles after entrainment in the airstream.

5.0 RECOMMENDATIONS

It is recommended that the work described in this report be continued. Specifically, the following are recommended:

1. Investigate the function of compaction in the mechanisms of surface erosion.
2. Investigate the function of particle rotation during entrainment.
3. Quantitatively define the effect of surface roughness on aerodynamic shear stress.
4. Define particle departure angle as a function of gas flow dynamic pressure.
5. Define particle velocity as a function of gas flow dynamic pressure.
6. Investigate different surface particulate material.
7. Investigate a larger range of particle size distributions and surface roughness profiles.
8. Investigate the possibility of electrostatic generation in a saltation layer.

APPENDIX A

DERIVATION OF EQUATION

Since, by definition, shearing stress is simply the ratio of a force acting tangentially on an area to that area

$$\tau_t = \frac{F_t}{A} \tag{A1}$$

it was decided to expose a surface to a range of air flows in the McDonnell Douglas Surface Erosion Simulator, measure the tangential force acting on that surface, and calculate the shearing stress using Equation A1.

In practice, however, the test surface was prepared on a flat plate, mounted in the erosion simulator wind tunnel at the center line, exposed to an air flow, and the total force acting on the surface model and model support struts measured. Therefore, it was necessary to differentiate the tangential force acting on the test surface from all other forces on the model and support struts.

It was assumed that the forces on the model, excluding the test surface, and the forces on the support struts would be constant functions of the gas flow dynamic pressure because their exposed area configurations would be unchanging. As a result, the tangential force on the test surface could be determined by

$$F_t = F_T - F_b - F_s \tag{A2}$$

where F_t is the tangential force on the test surface, F_T is the total tangential force on the exposed system, F_b is the tangential force on the model excluding the test surface, and F_s is the aerodynamic force on the support struts.

Values for the two forces F_b and F_s were determined for a range of gas flow dynamic pressures and curve fit by the method of least squares. They were found to be, respectively

$$F_b \text{ (lb)} = 1.04\ q_\infty \text{ (lb/in}^2\text{)} + 2.82 \times 10^{-3} \tag{A3}$$

and

$$F_S \text{ (lb)} = 2.563\ q_\infty \text{ (lb/in}^2\text{)} \qquad \text{(A4)}$$

where q_∞ is the air flow dynamic pressure. It may be seen that the force in Equation A3 does not go to zero with the air flow dynamic pressure as one would expect. This is the result of both the inherent experimental error and the curve fit technique. However, the calculated force (Equation A3) values were in close agreement to the original data so it was concluded that Equation A3 was valid for the parameters investigated.

Therefore, combining Equations A2, A3, and A4, the tangential force on the test surface is

$$F_t \text{ (lb)} = F_T - [3.603\ q_\infty \text{ (lb/in}^2\text{)} + 2.82 \times 10^{-3}] \qquad \text{(A5)}$$

and by Equation A1, the shear stress is

$$\tau_t \text{ (lb/in}^2\text{)} = 6.94 \times 10^{-3}\ F_T \text{ (lb)} - [2.50 \times 10^{-2}\ q_\infty \text{ (lb/in}^2\text{)} + 1.96 \times 10^{-5}] \qquad \text{(A6)}$$

Equation A6 is used for all experimental shear stress calculations in this investigation.

APPENDIX B

ERROR ANALYSIS

In order to assess the validity of the experimental results, an error analysis[44] was performed on q_∞, τ_t, and $\bar{V}_p$. The probable error in q_∞ can be written.

$$P(q_\infty) = \left\{ \left(\frac{\partial q_\infty}{\partial P_s} \right)^2 \delta^2 P_s + \left(\frac{\partial q_\infty}{\partial P_i} \right)^2 \delta^2 P_i + \left(\frac{\partial q_\infty}{\partial \gamma} \right)^2 \delta^2 \gamma \right\}^{\frac{1}{2}} \tag{B1}$$

However, if γ is taken as a constant, $\delta\gamma = 0$ and

$$P(q_\infty) = \left\{ \left(\frac{\partial q_\infty}{\partial P_s} \right)^2 \delta^2 P_s + \left(\frac{\partial q_\infty}{\partial P_i} \right)^2 \delta^2 P_i \right\}^{\frac{1}{2}} \tag{B2}$$

where

$$\frac{\partial q_\infty}{\partial P_s} = \frac{q_\infty}{P_s} - \frac{P_i}{P_s} \left[\frac{P_s + P_i}{P_s} \right]^{-\frac{1}{\gamma}}$$

and

$$\frac{\partial q_\infty}{\partial P_i} = \left[\frac{P_s + P_i}{P_s} \right]^{-\frac{1}{\gamma}}$$

Substituting the above into Equation B2, the probable error in q_∞ is

$$P(q_\infty) = \left\{ \left(\frac{q_\infty}{P_s} - \frac{P_i}{P_s} \left[\frac{P_s + P_i}{P_s} \right]^{-\frac{1}{\gamma}} \right)^2 \delta^2 P_s + \left(\left[\frac{P_s + P_i}{P_s} \right]^{-\frac{1}{\gamma}} \right)^2 \delta^2 P_i \right\}^{\frac{1}{2}} \tag{B3}$$

where the uncertainties or errors in P_s and P_i can be estimated or obtained directly from the data.

Similarly, the probable errors in τ_t and $\bar{V}_p$ are, respectively,

$$P(\tau_t) = \left\{ (4.816 \times 10^{-5}) \, \delta^2 F_T + (6.25 \times 10^{-4}) \, \delta^2 q_\infty \right\}^{\frac{1}{2}} \tag{B4}$$

and

$$P(\bar{V}_p) = \left\{ \frac{\delta^2 \ell_o + \delta^2 \ell_1}{(t_1 - t_o)^2} + \frac{(\ell_1 - \ell_o)^2}{(t_1 - t_o)^4} \left(\delta^2 t_o + \delta^2 t_1 \right) \right\}^{\frac{1}{2}} \tag{B5}$$

APPENDIX C

FRICTION COEFFICIENTS CALCULATED FROM EXPERIMENTAL DATA USING ROBERTS' THEORY

INTRODUCTION

This appendix presents friction coefficients calculated from the McDonnell Douglas experimental data observed near threshold conditions for smooth and rough particle-covered surfaces. Roberts' Theory and the method used to compute friction coefficients are presented first, followed by results calculated from experimental data.

DISCUSSION

Roberts[24-25] has evolved a theoretical model to describe the erosion and subsequent transport of dust in the vicinity of a rocket exhausting normal to a surface in near-vacuum conditions. He formulates that the coefficients of friction, C_f, relates the aerodynamic shear stress acting on a surface to the gas flow dynamic pressure over the surface by

$$\tau = C_f q \tag{C1}$$

and that the rate of soil erosion is given by

$$\tfrac{1}{2}\, a u \sigma c \cos\beta \frac{\partial y}{\partial t} = \tau - \tau^* \tag{C2}$$

where "a" is a momentum factor, u is the gas radial velocity, σ is the soil mass density, c is the packing constant, β is the surface slope, y is the depth of erosion, t is time, τ is the aerodynamic shear acting on the surface, τ^* is the surface shear resistivity, q is the gas flow dynamic pressure, and C_f is the coefficient of friction which is essentially constant and equal to 0.2.

If test data are used, Equation C1 can be solved to generate values of C_f and curve fit by the method of least squares to define C_f as a function of gas flow dynamic pressure.

RESULTS

Two methods of grouping the smooth and rough surface test data (Figures 9 through 12) were used to compute C_f. One method required computing C_f for each particle size range and surface profile. The other method required computing a general C_f for each of the two surface profiles. The results are given in Table C1 and indicate that the coefficient of friction is greater for the rough surface, and is smaller than Roberts' value of 0.2 by an order of magnitude.

On the other hand, a mathematical investigation by R. E. Hutton[32] found the average coefficient of friction to be greater than 0.2. He introduced test data, obtained from a study of a supersonic jet impinging on a flat particle-covered surface in near-vacuum conditions[23], into Roberts' formulae and computed values for C_f as a function of radial station and time. He found the averages for a surface of glass beads were 0.854, 1.30, 1.47 and for gravel 3.14.

TABLE C1 EXPERIMENTAL FRICTION COEFFICIENT VALUES

DYNAMIC SURFACE PROFILE	SURFACE PARTICLE SIZE DISTRIBUTION (MICRONS)	THRESHOLD GAS DYNAMIC PRESSURE q_∞ (LB/IN.^{2})	C_f TERM (LEAST SQUARES METHOD)		C_f VALUE AT THRESHOLD q_∞	
			EACH PARTICLE SIZE GROUP	EACH SURFACE PROFILE	EACH PARTICLE SIZE GROUP	EACH SURFACE PROFILE
SMOOTH	1–500	3.40×10^{-3}	$1.96 \times 10^{-2} - 1.19\ (q_\infty)$	$1.756 \times 10^{-2} - 0.991(q_\infty)$	1.55×10^{-2}	1.419×10^{-2}
	177–210	2.27	$1.817 \times 10^{-2} - 1.103(q_\infty)$		1.567	1.531
	53–63	1.08	$1.61 \times 10^{-2} - 0.81\ (q_\infty)$		1.523	1.649
	1–44	0.94×10^{-3}	$1.728 \times 10^{-2} - 1.051(q_\infty)$		1.629×10^{-2}	1.663×10^{-2}
ROUGH	1–500	3.32×10^{-3}	$2.03 \times 10^{-2} + 0.298(q_\infty)$	$2.137 \times 10^{-2} - 0.260(q_\infty)$	1.93×10^{-2}	2.051×10^{-2}
	177–210	1.99	$3.28 \times 10^{-2} - 1.07\ (q_\infty)$		3.067	2.085
	53–63	1.34	$1.65 \times 10^{-2} + 0.845\ (q_\infty)$		1.537	2.102
	1–44	1.20×10^{-3}	$1.51 \times 10^{-2} + 0.991\ (q_\infty)$		1.629×10^{-2}	2.106×10^{-2}

APPENDIX D

EXPERIMENTAL DATA AND BAGNOLD'S THEORY

INTRODUCTION

This appendix presents threshold erosion parameters calculated from the McDonnell Douglas experimental data observed near threshold conditions using Bagnold's Theory. Bagnold's Theory and the method used to compute parametric values are presented first, followed by results calculated from experimental data.

DISCUSSION

Bagnold[6] found that under steady flow conditions over flat surfaces, the wind drag or aerodynamic shear stress and the wind velocity above the surface are given by

$$\tau = \rho_\infty V^2_* \tag{D1}$$

and

$$v = 5.75 V_* \log_{10} \frac{z}{k} \tag{D2}$$

where τ is the aerodynamic shear stress per unit area, ρ_∞ is the wind density, v is the wind velocity measured at any height z, k is a surface roughness parameter, and V_* is the wind "shear velocity."

He established that the wind shear velocity is proportional to the rate of wind speed with log-height and could be determined by physically measuring the wind velocity at any two known heights, plotting these velocities against log-height, and drawing a straight line through the resulting points. The velocity difference between any two heights of which one is ten times the the other then yields 5.75 V_*. Furthermore, the surface roughness parameter, called the height of focus, could be determined by extrapolating the straight line to the axis of zero velocity. The height above the surface at which zero velocity occurs is

the "height of focus" and is approximately equal to 1/30 of the diameter of the surface particles.

Bagnold also observed that surface particles are put into motion when the wind shear velocity just exceeds a critical value, called the "threshold shear velocity", which is a function of the particle diameter. If the Reynolds number close to the surface is greater than 3.5 ($V_* d/\nu > 3.5$), this threshold shear velocity varies as the square root of the particle diameter according to

$$V_{*_t} = A\sqrt{\frac{\sigma - \rho_\infty g d}{\rho_\infty}} \qquad (D3)$$

where V_{*_t} is the threshold shear velocity, A is a constant equal to 0.1 for air, σ is the particle material density, ρ_∞ is wind density, g is the acceleration of gravity, and d is the particle diameter. If, however, the Reynolds number close to the ground is less than 3.5 ($V_{*d}/\nu < 3.5$), the flow very close to the surface begins to obey different laws and the coefficient A is no longer constant, but increases as particle size decreases.

If test data are used, Equations D1, D2 and D3 can be solved to generate theoretical values of the wind velocity and aerodynamic shear stress required to initiate surface erosion. In addition to this, if the wind velocity is measured at any two known heights just before surface erosion is initiated, and the wind shear velocity is computed by the graphical method described above, Equations D1 and D2 can be solved to generate theoretical values of the actual threshold wind velocity and aerodynamic shear stress.

RESULTS

The McDonnell Douglas experimental data, Bagnolds' experimental observations, and the theory-calculated data are given in Figure D1 and Tables D1 through D3. The air flow data are presented both as wind velocity and wind dynamic pressure

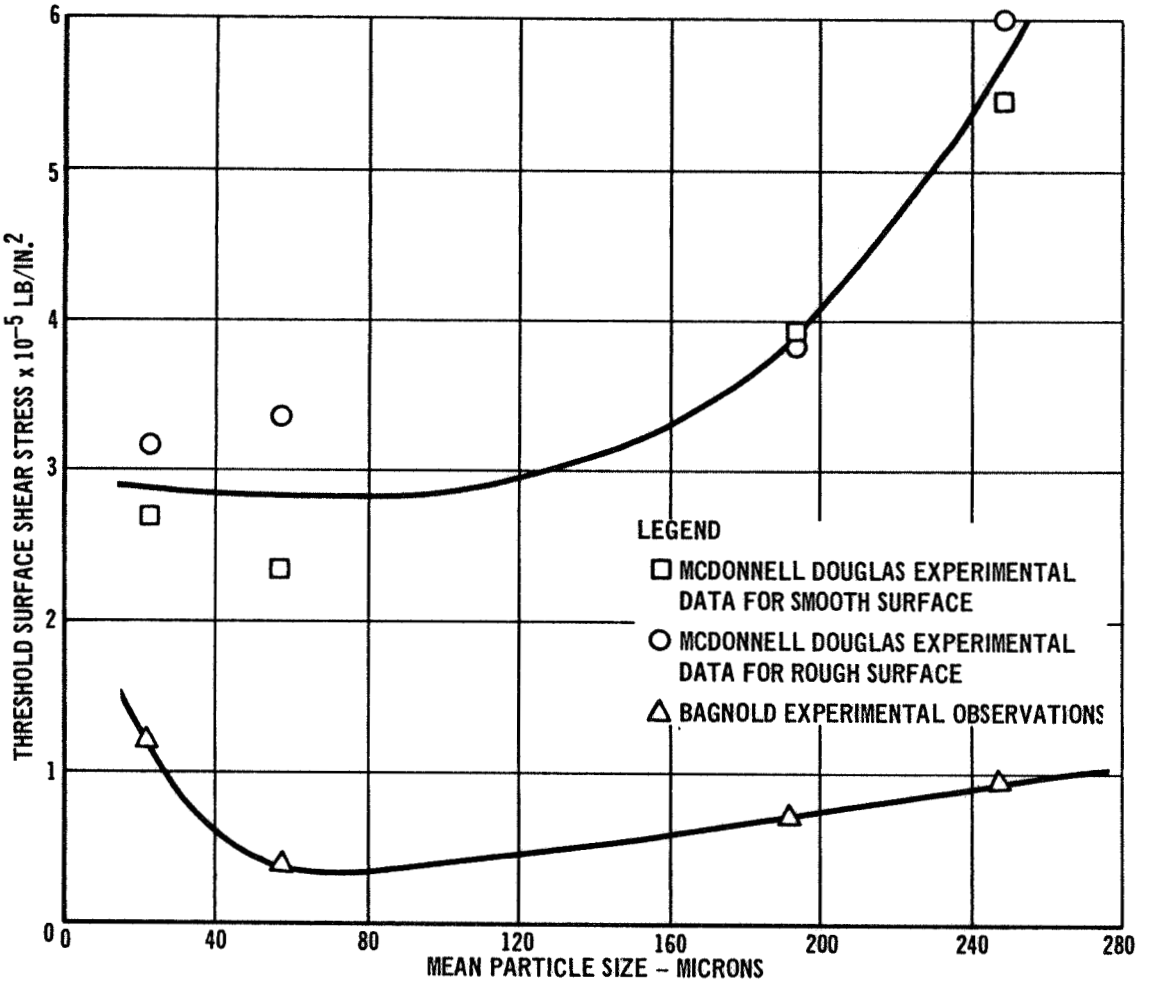

FIGURE D1 EXPERIMENTAL THRESHOLD SURFACE SHEAR STRESS

TABLE D1 THRESHOLD VELOCITY

SURFACE / INVESTIGATOR		MCDONNELL DOUGLAS	BAGNOLD	MCDONNELL DOUGLAS DATA USING BAGNOLD'S THEORY	
PROFILE	SIZE DISTRIBUTION (MICRONS)	EXPERIMENTAL OBSERVATION (FT/SEC)	EXPERIMENTAL OBSERVATION (FT/SEC)	$V_{*_t} = 0.1\sqrt{\frac{\sigma - \rho_\infty}{\rho_\infty} gd}$ $k = d/30$ (FT/SEC)	V_* AND k FROM VELOCITY PROFILE (FT/SEC)
SMOOTH	1–500	356	15.2	268	385
	177–210	318	13.8	268	357
	53–63	275	11.9	213	295
	1–44	264	22.3	146	257
ROUGH	1–500	373	–	303	378
	177–210	307	–	256	294
	53–63	333	–	234	311
	1–44	313	–	160	338

TABLE D2 THRESHOLD DYNAMIC PRESSURE

SURFACE / INVESTIGATOR		MCDONNELL DOUGLAS	BAGNOLD	MCDONNELL DOUGLAS DATA USING BAGNOLD'S THEORY	
PROFILE	SIZE DISTRIBUTION (MICRONS)	EXPERIMENTAL OBSERVATION ($LB/IN.^2$)	EXPERIMENTAL OBSERVATION ($LB/IN.^2$)	$V_{*_t} = 0.1\sqrt{\frac{\sigma - \rho_\infty}{\rho_\infty} gd}$ $k = d\ 30$ ($LB\ 'IN.^2$)	V_* AND k FROM VELOCITY PROFILE ($LB/IN.^2$)
SMOOTH	1–500	3.40×10^{-3}	1.89×10^{-3}	1.93×10^{-3}	3.98×10^{-3}
	177–210	2.27	1.56	1.60	2.83
	53–63	1.08	1.17	0.66	1.25
	1–44	0.94×10^{-3}	4.08×10^{-3}	0.29×10^{-3}	0.89×10^{-3}
ROUGH	1–500	3.32×10^{-3}	–	2.21×10^{-3}	3.42×10^{-3}
	177–210	1.99	–	1.40	1.84
	53–63	1.34	–	0.67	1.19
	1–44	1.20×10^{-3}	–	0.32×10^{-3}	1.43×10^{-3}

TABLE D3 THRESHOLD SURFACE SHEAR STRESS

SURFACE \ INVESTIGATOR		MCDONNELL DOUGLAS	BAGNOLD	MCDONNELL DOUGLAS DATA USING BAGNOLD'S THEORY	
PROFILE	SIZE DISTRIBUTION (MICRONS)	EXPERIMENTAL OBSERVATION (LB/IN.^{2})	EXPERIMENTAL OBSERVATION (LB/IN.^{2})	$V_{*_t} = 0.1\sqrt{\frac{\sigma - \rho_\infty}{\rho_\infty} gd}$ (LB/IN.^{2})	V_* FROM VELOCITY PROFILE (LB/IN.^{2})
SMOOTH	1–500	5.50×10^{-5}	0.941×10^{-5}	0.960×10^{-5}	9.70×10^{-5}
	177–210	3.95	0.731	0.745	7.15
	53–63	2.35	0.398	0.224	2.78
	1–44	2.70×10^{-5}	1.20×10^{-5}	0.084×10^{-5}	2.57×10^{-5}
ROUGH	1–500	6.05×10^{-5}	–	0.961×10^{-5}	15.70×10^{-5}
	177–210	3.89	–	0.745	22.08
	53–63	3.37	–	0.221	9.78
	1–44	3.16×10^{-5}	–	0.084×10^{-5}	8.52×10^{-5}

($q_\infty = \frac{1}{2} \rho_\infty v^2$) to insure a meaningful comparison because Bagnold observed terrestial winds approximately equal to 1.22×10^{-3} gm/cm^3 in density, while McDonnell Douglas investigated rarified air flows ranging from 1.0 to 20.0 x 10^{-6} gm/cm^3 in density.

APPENDIX E

REFERENCES

1. Statement of Work for Task Order Four, "Surface Erosion Due to Retro-Rocket Exhaust Gas Impingement" of Master Agreement Contract NAS1-8137, "Analysis, Design, and Fabrication of Landing Impact Test Vehicles for Unmanned Planetary Landing," National Aeronautics and Space Administration, Langley Research Center, Hampton, Virginia.
2. Cramblit, D. C., "A Consideration of Lunar Surface Ballistics and the Hazards Associated with Spacecraft Landing or Launch Operations," NASA TN D-1526.
3. Hutton R. E., "Lunar Surface Erosion During Apollo 11 Landing," TRW Systems Group Report 11176-6068-R0-00, 20 Nov. 69.
4. NASA Manned Space Center, "Apollo 11 Preliminary Science Report," NASA SP-214.
5. NASA Manned Space Center, "Apollo 12 Preliminary Science Report," NASA SP-235, 1 June 70.
6. Bagnold, R. A., The Physics of Blown Sand and Desert Dunes, Methuen Ltd., 1941.
7. Bird, Warren, and Lightfoot, Transportation Phenomena, J. Wiley and Sons, 1960.
8. Chepil, W. S., "Dynamics of Wind Erosion: I. Nature of Movement of Soil by Wind," Soil Science, Vol 60, PP 305-320, 1945.
9. Chepil, W. S. "Dynamics of Wind Erosion: II. Initiation of Soil Movement," Soil Science, Vol 60, PP 397-411, 1945.
10. Chepil, W. S., "Equilibrium of Soil Grains at the Threshold of Movement by

Wind," Soil Science Society of American Proceedings, Vol. 23, No. 6, p.p. 422-428, 1959.

11. Hilst, G. R., and Nickola, P. W., "On the Wind Erosion of Small Particles," Bulletin American Meteorological Society, Vol. 40, No. 2, 1959.

12. Kadib, A. A., "Function for Sand Movement by Wind," Hydraulic Engineering Laboratory Report HEl 2-12, University of California, 1965.

13. Kawamura, R. "Study of Sand Movement by Wind," Report of The Institute of Science and Technology, University of Tokyo, Vol 5 No 3/4, Oct 1951.

14. Obrian, M. P., and Rindlamp, B. D., "The Transportation of Sand by Wind," Civil Engineering, May 1936.

15. Owen, P. R., "Saltation of Uniform Grains in Air," Journal of Fluid Mechanics, Vol. 20, Part 2, p.p. 225-242, 1964.

16. Punjrath, J. S., and Heldman, D. R., "Mechanisms of Small Particle Reentrainment From Flat Surfaces," Paper presented at 9th Annual Technical Meeting and Exhibit American Association for Contamination Control, Anaheim, California, 19-22 April 1970.

17. Yves Bellx, P., "Sand Movement by Wind, U.S. Army Coastal Engineering Research Center TM1, 1964.

18. Zingg, A. W., A Study of the Characteristics of Sand Movement by Wind, A Thesis, Kansas State College of Agriculture and Applied Science, Department of Agricultural Engineering.

19. Shuter, D. V., An Analysis of Ground Erosion Caused by Jet Downwash Impingement, United States Naval Postgraduate School Thesis, 1965.

20. Vidal. R. J., Aerodynamic Processes in the Downwash--Impingement Problem, Cornell Aeronautical Laboratory, Inc., 15 Feb. 1962.

21. Grossman. R. L., "Characteristics of Particles Blown Away by Exhaust Jet

Impingement on a Lunar Surface," AIAA Paper 63-199, 1963.

22. Hurt, Jr., G. J., and Lina, L. J., "Blast Effects of Turn Variable-Cant Rocket Nozzles on Visibility During Landing on a Particle-Covered Surface," NASA TN D-2455.

23. Land, N. S., and Conner, D. W., "Laboratory Simulation of Lunar Surface Erosion by Rockets," NASA TMX-59863, 1967.

24. Roberts, L., "The Action of a Hypersonic Jet on a Dust Layer," IAS Paper 63-50, 1963.

25. Roberts, L. "Exhaust Jet-Dust Layer Interaction During a Lunar Landing," XIIIth International Astronautical Congress Proceedings I, Varna, 1962.

26. Spady, Jr., A. A., "An Exploratory Investigation of Jet-Blast Effects on a Dust-Covered Surface at Low Ambient Pressure," NASA TN D-1017, Feb. 1962.

27. Stitt, L. E., "Interaction of Highly Underexpanded Jets with Simulated Lunar Surfaces," NASA TN D-1095.

28. Adlon, G. L., Weinberger, R. K., and McClure, D. R., "Martian Sand and Dust Storm Simulation and Evaluation," NASA CR-66882, 31 Oct. 1969.

29. Hertzler, R. G., "Particle Behavior in a Simulated Martian Environment," McDonnell Aircraft Co. Report E418, 1966.

30. Hertzler, R. G., "Behavior and Characteristics of Simulated Martian Sand and Dust Storms," McDonnell Aircraft Co. Report E720, 1966.

31. Hutton, R. E., "LM Soil Erosion and Visibility Investigations Part I and II," TRW System Group Report 11176-6060-R0-00, 13 Aug. 1969.

32. Hutton, R. E., "Comparison of Soil Erosion Theory with Scaled LM Jet Erosion Tests," NASA CR-66704, Oct. 1968.

33. Personal Communication with R. E. Hutton, 17 Dec. 1969.

34. NASA Viking Project Office, "Mars Engineering Model," Document No. M72-106-0, 1969.

35. NASA Photographs AS11-45 6705 A & B.

36. NASA Photographs AS11-45 6706 A & B.

37. NASA Photographs AS11-45 6708 A & B.

38. NASA Photographs AS11-45 6712 A & B.

39. NASA Photographs AS11-45 6998 A & B.

40. NASA, "Apollo 11 Preliminary Science Report," NASA SP 214, Clearinghouse, 1969.

41. NASA, "Apollo 12 Preliminary Science Report," NASA SP 235, Clearinghouse, 1970.

42. Goldstein, S., Modern Developments in Fluid Dynamics, Vol I, p.p. 135-139, Dover Publications, New York, 1965.

43. Goldstein, S., Modern Developments in Fluid Dynamics, Vol I, p.p. 316-319, Dover Publications, New York, 1965.

44. Beers, Y., Introduction to the Theory of Error, Addison-Wesley Publishing Co., 1957.

Particle Dislodgement and Entrainment By a Low Density Air Stream Flowing Over a Surface

NASA CR-111924
Particle Dislodgement and Entrainment
By A Low Density Airstream Flowing
Over A Surface

R. K. Weinberger, G. L. Adlon
August 6, 1971

I R. K. Weinberger
II G. L. Adlon
III NASA CR-111924

ABSTRACT

An experimental technique was developed and a preliminary investigation made of the dislodgement and subsequent entrainment of solid particles by a stream of low density air flowing over a particulate surface. Four size ranges of solid particles and two surface profiles were tested. At the inception of surface erosion the following were determined: airstream dynamic pressure, airstream density, aerodynamic shear stress on the surface and/or surface resistivity, particle departure angle, and particle departure velocity. In addition, the entrained particles were trapped at several heights above the surface and the size distributions determined.